Lin *et al. Chem. Synth.* **2025**, *5*, 37
DOI: 10.20517/cs.2024.53

Chemical Synthesis

Review

Open Access

Check for updates

Synthesis and regulation strategies for enhancing the electrochemical performance of sodium-ion battery anode materials

Yuan-Ting Lin, Bi-Li Lin, Bai-Tong Niu, Xiao-Ping Chen, Hong-Xu Guo, Xiu-Mei Lin*

College of Chemistry, Chemical Engineering and Environment, Fujian Province Key Laboratory of Modern Analytical Science and Separation Technology, Minnan Normal University, Zhangzhou 363000, Fujian, China.

***Correspondence to:** Dr. Xiu-Mei Lin, College of Chemistry, Chemical Engineering and Environment, Fujian Province Key Laboratory of Modern Analytical Science and Separation Technology, Minnan Normal University, No. 36 Xianqianzhi Street, Xiangcheng District, Zhangzhou 363000, Fujian, China. E-mail: xiu-mei.lin@xmu.edu.cn

How to cite this article: Lin, Y. T.; Lin, B. L.; Niu, B. T.; Chen, X. P.; Guo, H. X.; Lin, X. M. Synthesis and regulation strategies for enhancing the electrochemical performance of sodium-ion battery anode materials. *Chem. Synth.* **2025**, *5*, 37. https://dx.doi.org/10.20517/cs.2024.53

Received: 19 Apr 2024 **First Decision:** 29 Jul 2024 **Revised:** 19 Aug 2024 **Accepted:** 13 Sep 2024 **Published:** 20 Mar 2025

Academic Editor: Xiang-Dong Yao **Copy Editor:** Pei-Yun Wang **Production Editor:** Pei-Yun Wang

Abstract

Rechargeable sodium-ion batteries (SIBs) have attracted increasing research interest because of their inherent advantages such as a similar working principle to lithium-ion batteries (LIBs) and plentiful, even-distributed, and inexpensive Na resources. However, Na ions possess a larger ionic radius (1.07 Å) compared to that of Li ions (0.76 Å), which brings key challenges such as irreversible capacity loss, sluggish kinetics, a considerable volume expansion, and low initial coulombic efficiency (ICE) of SIBs, especially for anodes. Despite these challenges, there have been ongoing efforts to develop various synthesis and regulation strategies to enhance the electrochemical performance of SIB anode materials and they are summarized here. In this review, the significance of developing SIBs, the types of SIB anode materials, and the key issues SIB anode materials face are discussed first. Then various developed synthesis and regulation strategies such as compositional, structural, and interfacial regulations based on different synthesis methods to enhance the electrochemical performance of SIB anode materials are summarized. Finally, in conclusions and outlooks**,** the present status of SIB anode materials is concluded and the future development directions are proposed.

Keywords: Sodium-ion battery anode materials, intercalation, conversion, alloying, compositional, structural, interfacial regulations

INTRODUCTION

Since the second industrial revolution, mankind has entered the electrical era and the use of electricity has entered a period of vigorous development. However, the excessive depletion of fossil fuels has resulted in resource and environmental issues. Thus, people have turned their attention to renewable energy such as solar and wind energy. The development and use of renewable energy have become a pivotal strategy in promoting the transformation of energy towards clean and low-carbon ways, as well as in ensuring energy security. However, these kinds of energy strongly depend on the natural environment and their supply is not stable, which has a great influence on the power supply if they are directly integrated into the power grid. Driven by this background and low-carbon and environmentally friendly production and lifestyle, new energy storage techniques represented by electrochemical energy storage, especially rechargeable batteries, are expected to become the core solution for large-scale grid-connection of renewable energy and smooth power grid fluctuations. Among various rechargeable batteries, lithium-ion batteries (LIBs) have an expansive range of applications within the energy market due to their elevated energy density and extended cycling lifespan. This is particularly the case in the field of power batteries; LIBs have a continuously expanding leading advantage[1-3]. Nevertheless, the limited and uneven distribution of Li resources within the earth's crust leads to relatively elevated costs, which poses great challenges to the ever-growing demand of the energy market[4,5]. Especially since 2021, the price of lithium carbonate has continued to run at a high level, making it challenging to support large-scale energy storage and the expanding electric vehicle market. Therefore, it is urgently and highly desired to develop supplement or alternative energy storage techniques of LIBs to relieve energy demand. Sodium-ion batteries (SIBs)[6-8], organic batteries[9,10], aqueous batteries[11,12], and other resource-rich, environmentally friendly, and sustainable rechargeable battery techniques therefore have attracted increasing research interest.

SIBs have shown appealing potential because of their advantages such as a similar working principle with LIBs, abundant, even-distributed, and low-cost sodium resources, and higher safety and superior electrochemical performance at low temperatures compared to LIBs. Currently, the energy density of the SIBs is about 100-150 $Wh{\cdot}kg^{-1}$ (the ternary LIBs is approximately 250 $Wh{\cdot}kg^{-1}$), and the cycle life of SIBs is around 65% of that of the LIBs. Although currently the energy density and cycle life of SIBs still lag behind those of LIBs, the resource, cost, safety, and low-temperature fast-charging advantages make SIBs a promising candidate to supplement or replace the applications of LIBs in some fields, such as energy storage power stations, electric vehicles, and start-stop batteries. As shown in Figure 1A, the structure and operational principles of SIBs are analogous to those of LIBs, mainly including a cathode, an anode, an electrolyte, and a separator. The cathode materials[13] of SIBs mainly include layered metal oxide[14], Prussian blue and its analogs[15], polyanion compounds[16], and oxalate-based[17], which have made a great development. However, as one of the fundamental components of SIBs, the electrochemical performance of anodes still requires improvement to match the performance of cathodes and thus facilitates the commercialization of SIBs[18].

Anode materials account for about 14% of the total cost of SIBs and their performance influences the overall performance of a full battery significantly. As can be observed in Figure 1B, based on the data obtained from the Web of Science, the publication numbers of SIB anodes have increased dramatically since 2014 due to their important role in energy development. The ideal SIB anode materials should satisfy the following criteria: (1) To obtain high volume-specific capacity and mass-specific capacity, an elemental mass of the anode materials should be light and density should be small and the material should be able to store as much Na^+ as possible; (2) The potential should be approximately equivalent to that of sodium metal to enhance the operating voltage of the full battery; (3) The electrode should be stable in the electrolyte; (4) It is essential that the materials display optimal electronic and ionic conductivity; (5) The materials employed

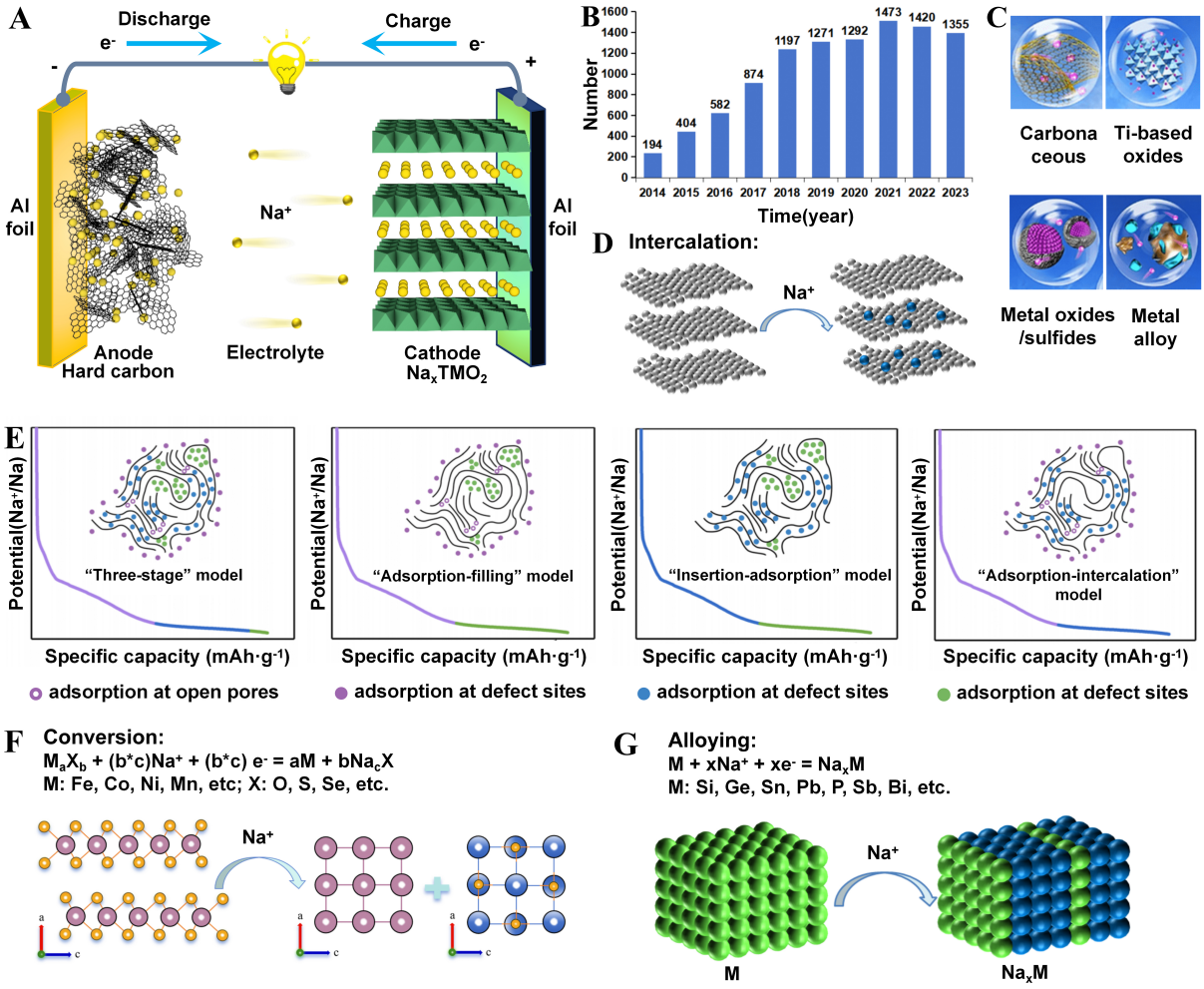

Figure 1. (A) Schematic diagram of the operational principle of SIBs; (B) Number of publications on SIB anodes in the past decade; (C) Different types of SIB anode materials. Quoted with permission from Huang *et al.*[6]; (D) Reaction mechanism schematics of intercalation. Quoted with permission from Qiao *et al.*[7]; (E) The mechanism of Na storage in HC. Quoted with permission from Chen *et al.*[19]; (F and G) Reaction mechanism schematics of conversion and alloying. Quoted with permission from Qiao *et al.*[7]. SIBs: Sodium-ion batteries; HC: hard carbon.

are sustainable, cost-effective, and environmentally friendly[8,16,18]. Currently, as shown in Figure 1C, there are three main types of anode materials based on their Na^+ storage mechanisms: intercalation, conversion, and alloying.

The intercalation type anode materials primarily consist of carbonaceous materials[19-21] and titanium-based oxides[22,23], in which the Na ions de/intercalate into the lattice of the materials for storage with negligible structural changes illustrated in Figure 1D. The stable structure of intercalation-type anode materials during the electrochemical de/sodiation process leads to good cycling stability. Carbonaceous materials mainly consist of graphite carbon and non-graphite carbon. Graphite carbon has a stable lamellar structure and excellent electrical conductivity. It has been successfully introduced to the market as an anode material for LIBs. However, it is challenging for Na ions to intercalate into the layers of graphite due to their bigger ionic radius compared to Li ions. Non-graphite carbon has amorphous structures, thus not having obvious characteristic graphite diffraction peaks. The interlayer spacing is larger, the presence of defects is more pronounced, and the microcrystalline structure is more disordered in comparison to graphite carbon, which

is favorable for the storage of Na-ion. According to the degree of graphitization, non-graphite carbon can be classified into soft carbon (SC) and hard carbon (HC)[19,20].

SCs are carbon materials that have undergone a high degree of graphitization after high temperature (over 2,800 °C) treatment while HC usually refers to carbon materials that are resistant to graphitization even under high-temperature treatment. SC includes carbon microspheres, needle coke, petroleum coke, *etc.* Compared to HC, SC exhibits a more ordered structure, a smaller interlayer spacing, a lower specific surface area, and a less microporous structure while these features are not conducive to sodium ion storage and diffusion. It has been reported that all SC materials suffer from insufficient sodium storage capacity (approximately 200 $mAh \cdot g^{-1}$) and a relatively high potential for sodium storage (exceeding 0.5 V *vs.* Na^+/Na). These factors impose significant limitations on the energy density of the Na-ion full-cell systems[1,4].

HC includes resin carbon, organic polymer pyrolytic carbon, carbon black, *etc.* It has a short-range ordered and long-range disordered structure, shows a graphite microcrystalline structure, and contains a high density of pores and defects. Based on these structural features, the main sodium storage active sites of HC include surface open pores, defect sites on graphite-like layers, interlayer spacing between graphite-like layers, and close cavities. Accordingly, there are four proposed sodium ion storage mechanisms: the "three-stage" model, "adsorption-filling" model, "insertion-adsorption" model, and the "adsorption-intercalation" model as illustrated in Figure 1E, for details please see the references[7,19,21]. The defects, disordered structure, and large layer spacing of HC synergistically improve its specific capacity. Additionally, HC has a low sodium storage potential (0.1 V *vs.* Na^+/Na) and is not soluble in electrolytes. Together with the features of broad resources, low cost, and environmental sustainability, HC becomes the most appealing and promising anode material of SIBs[20], whereas the significant quantity of defects of HC leads to irreversible Na^+ sites and thus has a relatively low initial coulombic efficiency (ICE) and an unsatisfied cycling life. Moreover, the disordered structure leads to relatively low conductivity and thus has an unsatisfied rate capability. Titanium-based oxides, which include TiO_2 and $Na_2Ti_3O_7$ (NTO), have become a crucial component of SIB anodes due to their structural stability, redox reaction potential platform stability (0.75 V *vs.* Na^+/Na), inexpensiveness, and environmental friendliness. However, inadequate electrical conductivity leads to tardy ion mobility and poor rate capability. Additionally, the titanium-based oxide anode materials have a low ICE as well[22,23].

The conversion-type materials mainly include transition metal sulfides (TMSs) and transition metal oxides (TMOs), which store Na^+ through conversion reactions. During the conversion reaction process, sodium ions replace transition metals and react with sulfur or oxygen in transition metal compounds to generate elemental transition metals and sodium sulfides or sodium oxides [Figure 1F]. The conversion reaction process involves the chemical transformation of one or more atoms, which is a phase transition reaction that involves the disruption and subsequent formation of chemical bonds, culminating in the creation of novel compounds. Due to the redox reactions involving multi-electron transfer during de/sodiation, conversion-type anode materials possess a high theoretical specific capacity ranging from 200-1,800 $mAh \cdot g^{-1}$[8]. However, the low electrical conductivity limits electron transport. Additionally, the large volume expansion/shrinking results in structural instability. The conversion type anode materials therefore have relatively limited rate capability and cycling stability[24-27]. Alloying-type anode materials include the elements of groups IV A and V A, for instance, P, Sn, Bi, Sb, Ge, *etc.* They have good electrical conductivity and very supernal theoretical specific capacity (847 and 2,596 $mAh \cdot g^{-1}$ of Tin and red phosphorus)[7].

However, the sodium storage process causes serious and irreversible volume expansion (200%-400%) [Figure 1G], resulting in pulverization of the electrode and rapid attenuation of specific capacity[28-30]. The

alloying-type materials therefore have poor cycling stability.

To solve the discussed problems of SIB anodes, it is essential to regulate the electrode materials and electrolytes to achieve enhanced electrochemical performance. The main regulation strategies include[31-40]: composition regulation, such as heteroatom doping, composite construction, and formation of heterostructure; structural regulation, such as nanostructure design, morphology control, and defect introduction; interfacial regulation, such as the regulation of electrode materials and electrolyte salts, solvents and additives to form a stable solid electrolyte interphase (SEI). In the following sections, various regulation strategies and their corresponding enhanced electrochemical performances of each type of SIB anode material will be introduced in detail with selected examples. It should be noted that most references in this review will focus on half-cells and it will be clarified when the data refer to the few full-cell cases. We aim to introduce versatile strategies for the optimization of sodium ion storage performance of anode materials.

COMPOSITIONAL REGULATIONS

Composition regulation mainly includes heteroatom doping, composite construction, and formation of heterostructure. Heteroatom doping refers to the introduction of heteroatoms or ions into a material to alter its microstructure, change its electronic state, and improve its electronic conductivity to improve its specific capacity and rate capability used as an anode material for SIBs[31,32,34]. In addition to heteroatom doping, incorporating porous carbon materials into anode materials to construct composite materials with improved ionic and electronic conductivity is also an effective strategy for obtaining high-performance anode materials. Furthermore, introducing a second or third component into anode materials to form heterogeneous structures can validly enhance the electrochemical performance of the anode materials due to the synergistic effect of all components[31-40]. The electrochemical performance of various SIB anode materials after compositional regulations is shown in Table 1.

HC

Pei *et al.* devised a novel protocol for *in-situ* texture creation utilizing sulfuric acid polymerized sucrose and trithiocyanuric acid as starting materials to fabricate N and S double-doped porous HC (SNC-P) material with increased layer spacing, appropriate doping and defect concentrations, thin carbon shells, and pore classification[41]. This material exhibited a notable reversible specific capacity of 430 and 277 mAh·g^{-1} at 0.05 and 5.0 A·g^{-1}, along with exceptional cyclic stability for Na^+ storage. Jin *et al.* synthesized N and S co-doped micro/nanoparticles as an anode material for SIB through a one-step approach involving thiourea and sodium citrate grounded on the pseudo-capacitance mechanism[42]. Upon fine-tuning, the specific capacity of NSC2 (thiourea to sodium citrate mass ratio of 2:1) was recorded as 280 and 223 mAh·g^{-1} at 0.05 and 1.0 A·g^{-1} after 200 and 2,000 cycles, respectively. Xie *et al.* implemented a successive carbonization process on the phosphate-treated petroleum residue to expunge the irreversible configuration of heteroatoms and delineate the screening strategy for heteroatom configuration shown in Figure 2A[43]. They retained the reversible heteroatom configuration and harmonized with free radicals, and the full battery achieved a consistently high slope capacity (250 mAh·g^{-1}) and ICE (80%) shown in Figure 2B. In the carbonization step following P/O doping, it was noted that the configuration of heteroatoms outweighs the amount of doping. Wu *et al.* synthesized N and P co-doped ultramicropores HC spheres (NPUCS) using polyvinyl alcohol (PVA) and sodium carboxymethyl cellulose as raw materials shown in Figure 2C[44]. The increase in the ratio of active pyridine-N had been found to enhance the electrode reactivity and Na^+ diffusion kinetics while reducing irreversible depletion. The NPUCS exhibited high specific capacity (257.7 and 157.0 mAh·g^{-1} at 0.1 and 5.0 A·g^{-1}) shown in Figure 2D, extraordinary ICE (75%) and stable Na storage performance (over 2,000 cycles).

Table 1. The electrochemical performance of various SIB anode materials after compositional regulations

Material	Mechanism	Regulation strategy	ICE (%)	Current density ($mA·g^{-1}$)	Cycles	Capacity retention ($mAh·g^{-1}$)	Ref.
PO-SC-S	Intercalation	Composition	80	750	2,000	249	[43]
NPUCS	Intercalation	Composition	75	5,000	2,000	110	[44]
NPDC (PDC-700)	Intercalation	Composition	44.4	2,000	2,000	197	[46]
NS-TiO_2	Intercalation	Composition	45.2	3,350	2,400	157.4	[48]
H-TiO_2@CFC	Intercalation	Composition	77.4	3,350	600	171.3	[50]
CC-ZnS/CNT	Conversion	Composition	82	5,000	500	314	[57]
Ni_3S_2-N-rGO 700 °C	Conversion	Composition	68	2,000	400	377	[59]
$Fe_7Ni_3S_{11}$/CN	Conversion	Composition	90	2,000	900	477	[61]
Sb_2O_3@Sb	Alloying	Composition	67.9	200	200	658	[63]
NP-SnSb	Alloying	Composition	60	200	240	388.1	[67]

SIB: Sodium-ion battery; ICE: initial coulombic efficiency; PO-SC-S: the pristine SC was co-doped with P/O and subsequently carbonized on two occasions at 800 °C; NPUCS: N and P co-doped ultramicropores HC spheres; NPDC: soybean roots-derived mesoporous HC constructed by N, P co-doping; NS-TiO_2: N and S double doping method to achieve highly doped anatase-type titanium; CNT: carbon nanotube; rGO: reduced graphene oxide; NP-SnSb: bimetallic nanoporous SnSb.

Mehmood *et al.* proposed a highly nanoporous (NP) carbon material doped with nitrogen created through the ionic carbonization of the Zn-imidazolium framework[45]. This material demonstrated a consistent cycling capacity of 496 and 280 $mAh·g^{-1}$ at 0.03 and 5.0 $A·g^{-1}$. Tao *et al.* produced mesoporous HC materials with N and P co-doping that were synthesized from soybean roots (NPDC)[46]. The material has abundant active sites, increased layer spacing, and a modified electronic structure. The pyrolysis of NPDC (NPDC-700) at 700 °C presented excellent rate capability (150 $mAh·g^{-1}$ at 5.0 $A·g^{-1}$) and exceptional cycle stability (197 $mA·g^{-1}$ at 2.0 $A·g^{-1}$ after 2,000 cycles). Yan *et al.* introduced an innovative synthesis technique for the fabrication of ultrahigh P-doped carbon (UPC) as an extraordinary-performance anode material for SIB[47]. By utilizing PCl_3 and cyclohexane (C_6H_{12}) as the sources of P and C, *in-situ* P-doping was achieved during carbonization under N_2 flow shown in Figure 2E, resulting in a phosphorus content up to 30 wt%. Moreover, the phosphorus incorporated in the carbon structure was mainly replaced by protrusions of P bonded to three C atoms [P-(C_3)], which can remarkably enhance the interlamellar spacing and improve the sorptive ability of Na^+. UPC-6 delivered a reversible capacity of 510.4 $mAh·g^{-1}$ at 0.1 $A·g^{-1}$ and an optimal rate capacity of 397.1 $mAh·g^{-1}$ at 10 $A·g^{-1}$ shown in Figure 2F.

Titanium-based oxides

Fan *et al.* used the N and S double doping method to achieve highly doped anatase-type titanium (NS-TiO_2) dioxide hollow spheres illustrated in Figure 3A[48]. The N doping reduced the band gap width of TiO_2 while the S doping promoted the spread of Na^+ in TiO_2. Therefore, TiO_2 co-doped with N and S exhibited significant electron conductance and accelerated Na^+ transfer kinetics. The tested material exhibited excellent rate performance and specific capacities of 249.3 and 156.4 $mAh·g^{-1}$ at 0.1675 and 5.025 $A·g^{-1}$, respectively. Additionally, it showed remarkable cycle stability with capacity retention of 90.5% at 3.35 $A·g^{-1}$ for 2,400 cycles illustrated in Figure 3B.

Studies have shown that incorporating porous carbon materials into TiO_2 to construct TiO_2@C composite material is conducive to enhancing the electronic/ionic conductivity of the composite material and is the most common and effective method to increase the electrochemical performance of titanium-based oxide anode materials. Luo *et al.* developed an anode material composed of TiO_2 nanoparticles anchored on the shear carbon nanotube backbone (TiO_2/SCNT), which demonstrated distinguished rate capability and cycling stability[49]. The TiO_2/SCNT electrode showed a specific capacity of 267 and 136 $mAh·g^{-1}$ at 1.0 and

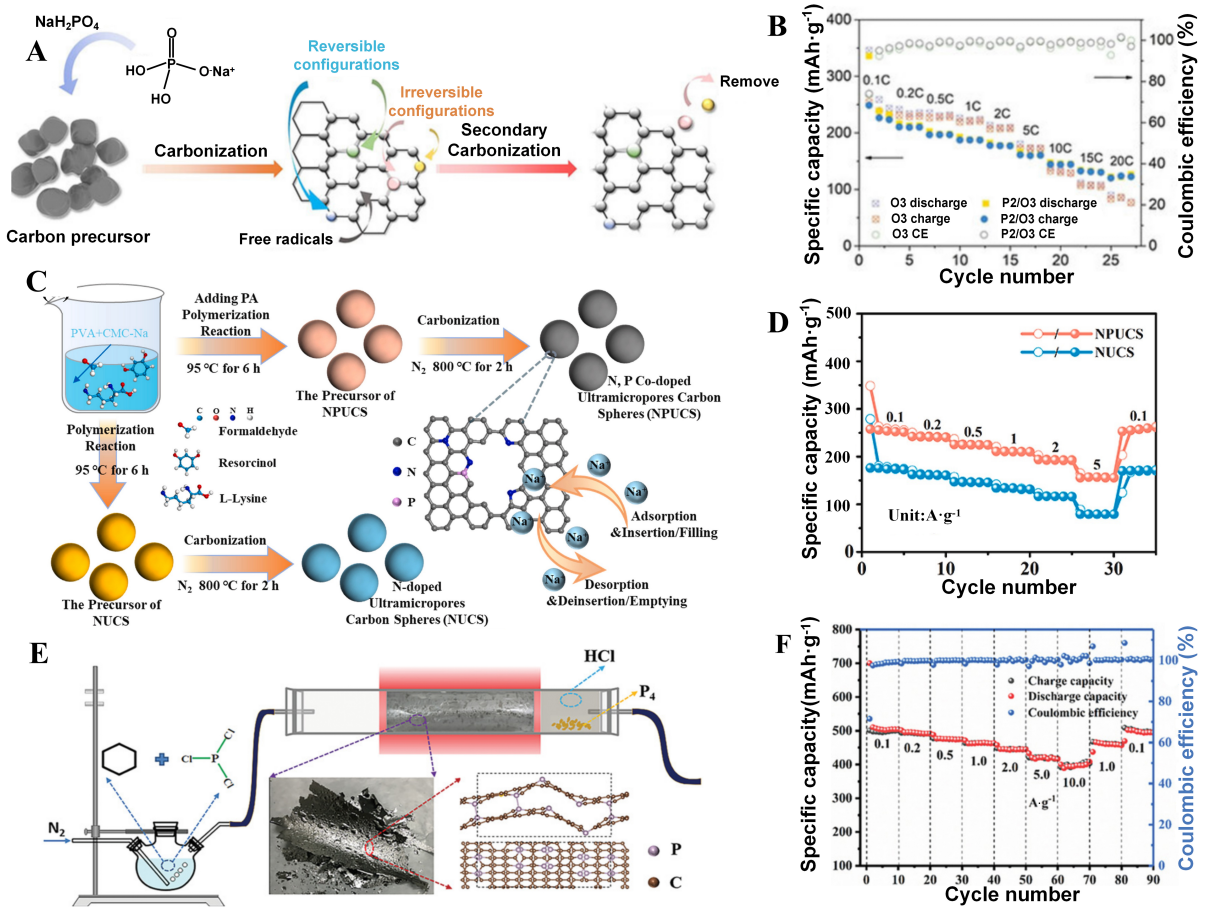

Figure 2. (A) Schematic illustration of the heteroatom configuration screening strategy for the synthesis of PO-SC-S as an anode material of SIBs and its corresponding (B) Rate performance of full cells coupled with an O3- or P2/O3-type cathode with C-rates from 0.1 to 20 C. Quoted with permission from Xie *et al.*[43]; (C) Synthesis scheme of NPUCS and NUCS and their corresponding (D) Rate capability. Quoted with permission from Wu *et al.*[44]; (E) Schematic illustration of the synthesis process of UPCs; (F) Rate capability of UPC-6. Quoted with permission from Yan *et al.*[47]. PO-SC-S: The pristine SC was co-doped with P/O and subsequently carbonized on two occasions at 800 °C; SIBs: sodium-ion batteries; NPUCS: N and P co-doped ultramicropores HC spheres; NUCS: N-doped ultramicropores carbon spheres; UPCs: UPC-6: phosphorus-doped carbon with molar ratios n (PCl_3) : n (C_6H_{12}) = 6:1; SC: soft carbon.

10 C and preserved 87% of the initial capacity for 1,000 cycles. Wang *et al.* outlined a technique for preparing carbon fiber clothing-supported rutile TiO_2 hollow cube array composites (H-TiO_2@CFC)[50]. This compound material served as a self-sustaining and binder-free anode for Na^+ storage, providing a reversible specific capacity of 287.3 and 103.3 mAh·g^{-1} at 0.1 and 50.0 C due to rapid ion dispersion and remarkable reactivity with Na^+.

The kinetics of Na^+ spread and its storage capacity within TiO_2 can be improved through the combination of heteroatom doping and composite material constructed with carbon. Lv *et al.* synthesized N/F co-doped TiO_2/carbon microspheres (NF-TiO_2/C) through a simple hydrothermal approach and high-temperature doping reaction[51]. The co-doping of N and F increased the content of oxygen vacancy (VO), narrowed the band gap between TiO_2 and C, and improved the conductivity of NF-TiO_2/C. Additionally, NF-TiO_2/C showed significant Na^+ bond energy and a low Na^+ diffusion barrier. Hence, NF-TiO_2/C provided a marked contact density (1.51 g·cm^{-3}), remarkable capacity (~242 mAh·g^{-1} at 1.0 C), excellent rate performance (190 and 125.9 mAh·g^{-1} at 10 and 100 C, respectively), high area capacity (~4.8 mAh·cm^{-2}) and very lasting cycle

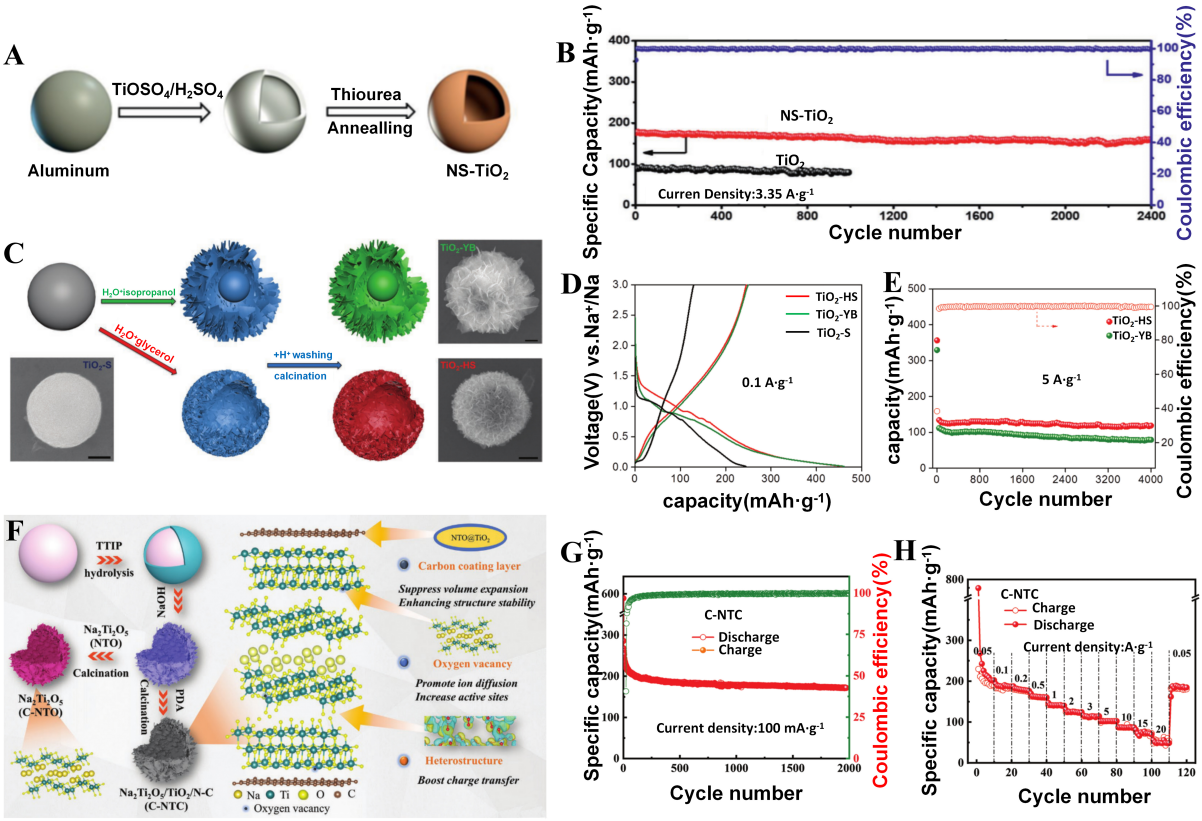

Figure 3. (A) Synthesis routes for NS-TiO_2; (B) Long-term cycle performance of TiO_2 and NS-TiO_2. Quoted with permission from Fan *et al.*[48]; (C) Synthesis routes for different TiO_2 spheres, and their corresponding (D) Initial charge/discharge profiles and (E) Long-term cycling performance. Quoted with permission from Xu *et al.*[54]; (F) Synthetic routes for C-NTO and C-NTC microspheres; (G) Cycling stability and (H) Rate performance of C-NTO. Quoted with permission from Meng *et al.*[55]; TiO_2-HS: TiO_2 hollow spheres formed by smaller nanosheets; TiO_2-YB: TiO_2 yolk-like spheres with bigger nanosheets; TiO_2-S: amorphous TiO_2 solid spheres; TTIP: tetra-n-butyl titanate; NS-TiO_2: N and S double doping method to achieve highly doped anatase-type titanium; NTO: $Na_2Ti_3O_7$; NTC: titanate/titanium.

performance (~80.2% at 10 C after 10,000 cycles). Wang *et al.* synthesized coadjacent micro-sheets composed of carbon nanotubes (CNTs) and S-doped TiO_2 (CNT/S-TiO_2) through ultrasonic technology followed by dead burn[52]. The use of single-wall CNTs (SWCNT) overcame the instability of electrode structure during the preparation of thick electrodes. CNT/S-TiO_2 showed an outstanding rate performance (0.3 to 15 C). Furthermore, the material exhibited long-cycle stability of enduring 1,000 cycles under a load of 1.96 mg·cm^{-2}.

Introducing different components into titanium-based materials to form heterogeneous structures can significantly enhance the conductivity of TiO_2. Guan *et al.* devised heterogeneous structures consisting of two-dimensional (2D) nanosheets TiO_2@$TiOF_2$ by hydrothermal method[53]. Among them, TiO_2@$TiOF_2$-30 h maintained a reversible capacity of 151.7 and 101.2 mAh·g^{-1} at 0.5 and 5.0 A·g^{-1} after 2,000 and 10,000 cycles. Density functional theory (DFT) simulations further showed that the hetero-structured TiO_2@$TiOF_2$ nanosheets had better electrical conductivity and lower Na^+ formation energy than separated TiO_2 and $TiOF_2$. Xu *et al.* developed a program to control the formation of hetero-structured TiO_2 spheres with an adjustable interior and shell shown in Figure 3C, which enhanced the pseudo-capacitive response and Na^+ storage dynamics and performance[54]. The rational design of nanosheets reduced the layered structure and generated excess space, thereby increasing the packing density of TiO_2 spheres. Among the

three TiO_2 spheres, TiO_2-HS had the highest surface area and the most exposed active surface and showed the most favorable electrochemical performance. The TiO_2-HS anode showed a significantly higher voltage plateau and lower polarization during the alkalization process shown in Figure 3D. At 5.0 $A·g^{-1}$ after 4,000 cycles, the TiO_2-HS electrode was still able to maintain a specific capacity of 119 $mAh·g^{-1}$ shown in Figure 3E. Meng *et al.* designed a sodium titanate/titanium dioxide/C (C-NTC) hetero-structural compound with VO shown in Figure 3F[55]. C-NTC electrodes achieved the optimal cycling performance with 172 $mAh·g^{-1}$ specific capacity after 2,000 cycles at 0.1 $A·g^{-1}$ shown in Figure 3G. At 0.05 $A·g^{-1}$, the specific capacity remained constant at 181.1 $mAh·g^{-1}$, with capacity retention reaching 90.6% after 120 cycles shown in Figure 3H.

Conversion-type materials

Compositing TMSs and TMOs with carbon materials to construct composites can effectively prevent the aggregation of metal nanoparticles, improve the interconnection between the nanoparticles, and enhance the electrical conductivity of the electrode materials, which leads to improved specific capacity, rate capability, and cycling stability. The formation of bimetallic or trimetallic composites can take advantage of the synergistic effect of heterogeneous metals and achieve the enhancement of the electrochemical performance of electrode materials.

Zhao *et al.* prepared ultrafine TMO nanoparticles encapsulated in nitrogen-doped carbon nanofibers (uf-TMOs@N-CNFs), in which polyvinylpyrrolidone (PVP) was utilized as a highly effective dispersant for inhibiting metal agglomeration and controlling the size of TMOs[56]. The uf-Fe_3O_4@N-CNFs offered a capacity of 234.5 $mAh·g^{-1}$ at 1.0 $A·g^{-1}$ with a contribution of 78.69% from pseudo-capacitor control. They also exhibited remarkable rate performance and durable cycle stability while retaining a capacity of 119.4 $mAh·g^{-1}$ after 5,000 cycles at 5.0 $A·g^{-1}$. Hou *et al.* described a TMSs-based covalent coupling strategy for anode material synthesis utilizing amide bonds to bind TMSs and CNTs shown in Figure 4A[57]. By forming a compact ZnS-CNT heterojunction to promote electron/ion transfer and ensure the stability of the structure shown in Figure 4B. The tight coupling interaction among ZnS and CNT resulted in the formation of the composite material with outstanding pseudo-capacitance behavior and highly reversible electrochemical process and thus had excellent electrochemical performance. It shows favorable specific capacity, rate capability, and cycling stability shown in Figure 4C-E. Chen *et al.* prepared SnS_2/FeS_2/reduced graphene oxide (rGO) composite by introducing FeS_2 *in situ* and growing SnS_2 simultaneously on rGO[58]. The composition and unique structure facilitated the expeditious dissemination of Na^+ and served to buffer the volume change. The test results indicated that the electrode had a specific capacity of 768.3 and 541.2 $mAh·g^{-1}$ at 0.1 and 1.0 $A·g^{-1}$.

Aminu Muhammad *et al.* successfully synthesized N-doped rGO (N-rGO) wrapped Ni_3S_2 nanocrystalline compound (Ni_3S_2-N-rGO-700 °C) through a simple phase conversion engineering process[59]. The strong coupling effect during annealing on the structural phase transition led to the formation of Ni_3S_2 nanocrystals and N-doped decreased graphene oxide nanocrystals, which significantly influenced the Na^+ storage properties of Ni_3S_2-N-rGO-700 °C nanocarbons. The Ni_3S_2-N-rGO-700 °C compound demonstrated a notably reversible capacity of 377 $mAh·g^{-1}$ at 2.0 $A·g^{-1}$. Furthermore, the system demonstrated a remarkably high level of coulombic efficiency, exceeding 100% over more than 400 cycles. Wang *et al.* developed N-doped hollow carbon nanospheres with uniformly embedded $MoSe_2$/Cr_2Se_3 heterojunction ($MoSe_2$/Cr_2Se_3@N-HCs) as SIB electrode materials shown in Figure 4F[60]. $MoSe_2$ and Cr_2Se_3 heterojunctions induced lattice mismatches at the hetero-structural interface, which contributed to spin-polarized surface capacitance. $MoSe_2$/Cr_2Se_3@N-HCS exhibited a striking capacity of 498 $mAh·g^{-1}$ at 0.1 $A·g^{-1}$ with outstanding durability over repeated cycles (405 $mAh·g^{-1}$ capacity after 1,000 cycles and a coulombic efficiency of 99.8%) shown in Figure 4G.

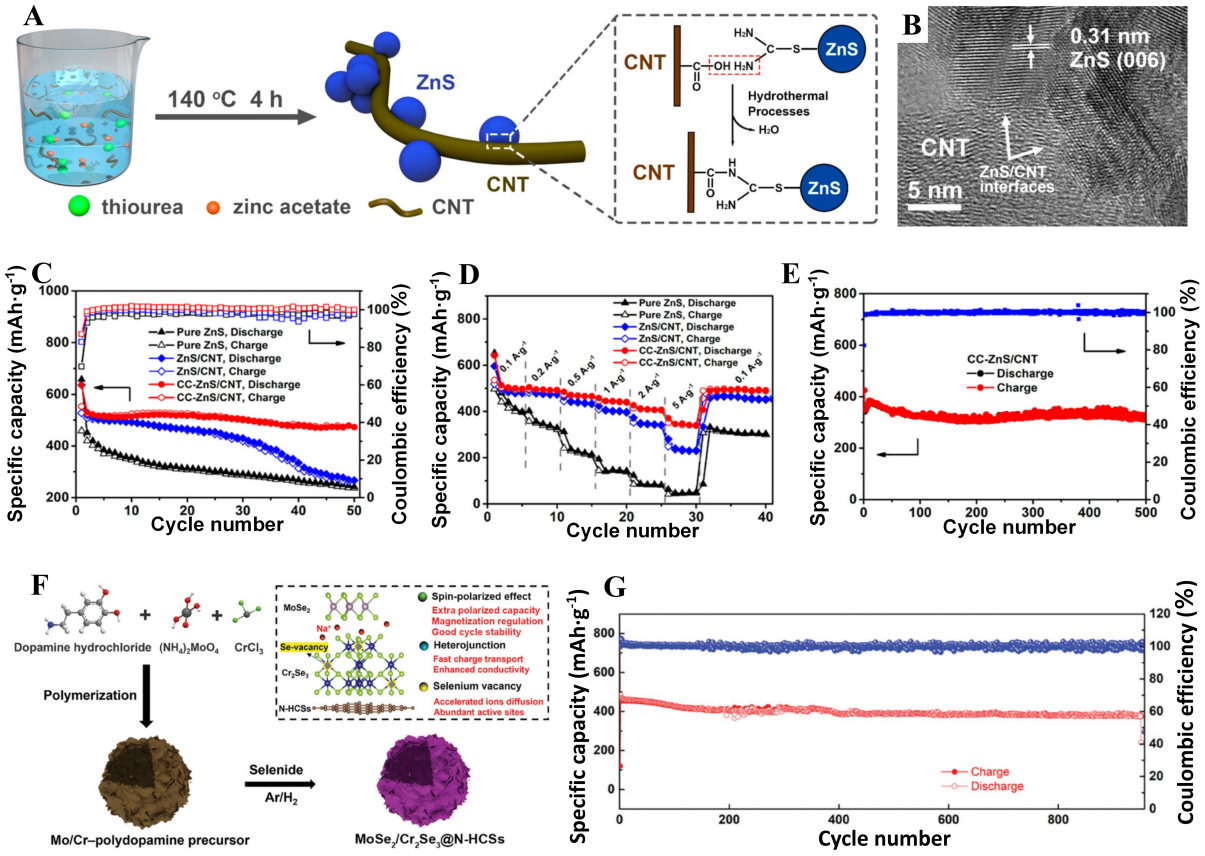

Figure 4. (A) Schematic illustration of synthesis procedure of the CC-ZnS/CNT and its corresponding (B) HRTEM image, (C) Cycling performance at 0.1 $A·g^{-1}$, (D) Rate capability compared with pure ZnS and ZnS/CNT, and (E) Long-term cycling performance at 2.0 $A·g^{-1}$. Quoted with permission from Hou *et al.*[57]; (F) Schematic representation depicting the synthesis process of the $MoSe_2/Cr_2Se_3$@N-HCSs; (G) Cycling stability of $MoSe_2/Cr_2Se_3$@N-HCSs in SIBs. Quoted with permission from Wang *et al.*[60]. CC-ZnS/CNT: Covalently coupled ZnS/CNT composite; HRTEM: high-resolution transmission electron microscopy; SIBs: sodium-ion batteries.

Chen *et al.* employed a one-step hydrothermal process followed by annealing to synthesize $Fe_7Ni_3S_{11}$/CN[61]. The resulting spherical solid solution $Fe_7Ni_3S_{11}$/CN had a hollow structure with ample active sites for Na^+ storage. Additionally, the $Fe_7Ni_3S_{11}$/CN nanoparticles were constrained by external CN, which promoted structural stability. The reversible specific capacity at 0.2 $A·g^{-1}$ was 567 $mAh·g^{-1}$. When exposed at 6.0 $A·g^{-1}$, $Fe_7Ni_3S_{11}$/CN maintained a capacity of 320 $mAh·g^{-1}$ over 5,000 cycles.

Alloying-type materials

Nanocomposites can mitigate volume expansion/shrinking of antimony-based materials during the de/sodiation process and improve their performance as an anode for SIB. Wang *et al.* proposed an innovative N-doped 3D porous carbon and studied the design and fabrication of network-confined nano-FeSb alloy composites (3DFeSb@NC) with robust Fe–N–C bonds[62]. This distinctive structure fully mitigated the volume change of Sb throughout the cycle, shortened the ion/electron proliferation distance, and enhanced the electrical conductivity. The 3D FeSb@NC anode had an excellent charge/discharge capability of 231 $mAh·g^{-1}$ at 5.0 $A·g^{-1}$ and adequate capacity retention of 85% after 750 cycles. Ma *et al.* synthesized an innovative Sb_2O_3@Sb nanocomposite with an ultra-fine Bi-continuous mesoporous structure shown in Figure 5A-C[63]. It demonstrated an exceptionally high specific capacity (659 $mAh·g^{-1}$ at 0.2 $A·g^{-1}$) in Figure 5D, overwhelming rate capacity (200 $mAh·g^{-1}$ at 29.7 $A·g^{-1}$), and outstanding cyclic stability with a capacity conservation rate of 99.8% after 200 cycles at 0.2 $A·g^{-1}$ shown in Figure 5E.

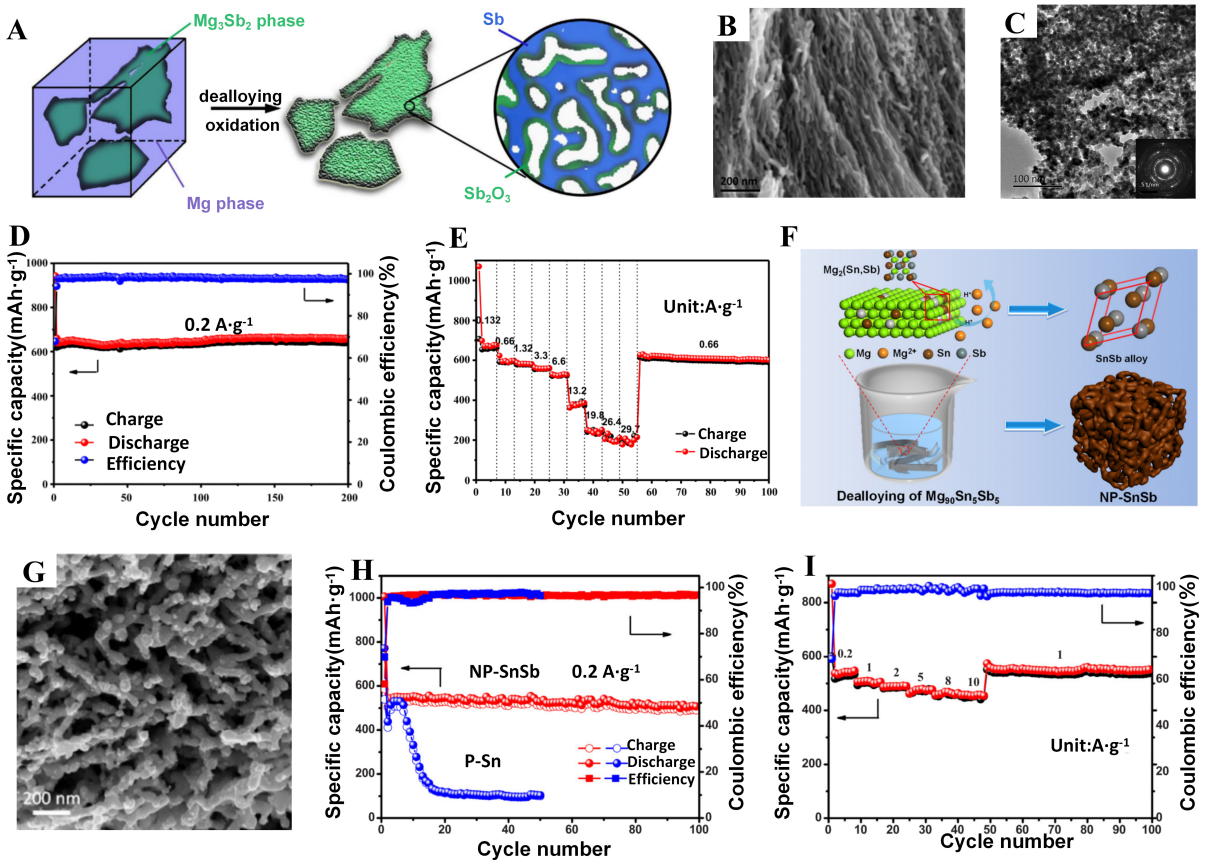

Figure 5. (A) Fabrication process of the mesoporous Sb_2O_3@Sb nanocomposite and its corresponding (B) SEM image, (C) TEM image, (D) Cycling performance, (E) Rate performance. Quoted with permission from Ma *et al.*[63]; (F) The one-step dealloying process for NP-SnSb alloy and its corresponding (G) SEM image; (H) Cycling performance (as benchmarked with P-Sn); (I) Rate performance at various specific currents. Quoted with permission from Ma *et al.*[67]. SEM: Scanning electron microscope; TEM: transmission electron microscopy; NP-SnSb: bimetallic nanoporous SnSb; P-Sn: porous Sn.

Edison *et al.* incorporated Fe into SnSb by rapid solidification technology to produce a novel ternary nanocrystalline composite, which effectively reduced the stress resulting from the conversion reaction, thereby enhancing the cyclic stability[64]. The SIB anode material provided a specific capacity of ~500 mAh·g^{-1} over more than 120 cycles at 0.5 A·g^{-1}. Chen *et al.* synthesized Bi nanoparticles embedded in an N-doped carbon matrix (Bi@NC)[65]. Even at 10 A·g^{-1}, Bi@NC electrodes still provide a high capacity of 338.2 mAh·g^{-1} (86% retained at 0.1 A·g^{-1}) and a high capacity of 326.9 mAh·g^{-1} after 5,000 cycles at 2.0 A·g^{-1}. Gao *et al.* successfully prepared NP Bi-Sb alloys with varying Bi/Sb ratios using Mg-based precursors[66]. Among them, the np-Bi_2Sb_6 electrode provided a reversible capacity of 257.5 mAh·g^{-1} after 2,000 cycles at 0.2 A·g^{-1} and exhibited long-term cycle performance at 1.0 A·g^{-1} with only 0.0072% capacity attenuation per 10,000 cycles. Ma *et al.* fabricated a bimetallic single-phase NP-SnSb alloy with a bicontinuous ligament channel structure shown in Figure 5F and G[67]. The NP-SnSb alloy had a special specific capacity [Figure 5H], with a reversible capacity of 506.6 mAh·g^{-1} after 100 cycles at 0.2 A·g^{-1}. Even at 10 A·g^{-1}, the reversible capacity can reach 458.2 mAh·g^{-1}, and when the specific current was reset to 1.0 A·g^{-1}, the reversible capacity fully recovered to 560.6 mAh·g^{-1} and remained stable for 100 cycles [Figure 5I]. Lei *et al.* successfully prepared heteroatomic amorphous phosphate-rich selenide molecules encapsulated in porous CNTs (a-P_9Se@pCNTs), which showed exceptional reversible Na^+ storage capacity with ICE up to 85.9% and specific capacity up to 2,215 mAh·g^{-1} at 0.2 A·g^{-1}[68]. Supplemented by DFT simulations and

comprehensive experimental studies, it was demonstrated that the low formation energy of Na products alleviated the issue of pulverization and prevented undesired decomposition.

STRUCTURAL REGULATIONS

Structural regulation, such as nanostructure design, morphology control, and defect introduction can create more active sites, shorten the distance of electron/ion transfer, promote ion diffusion and electron transfer, and relieve the strain of the volume extension in electrochemical de/sodiation and thus improve the electrochemical performance. Here, it should be noted that defect introduction is different from doping. It refers to the formation of non-ideal structures or states within a material, including lattice defects, vacancies, and edge defects to provide more storage sites/adsorption sites or to change the atomic structure and charge distribution of the material to promote ion diffusion and charge transfer and therefore to enhance the sodium ion storage performance[41-43]. The electrochemical performance of various SIB anode materials after structural regulations is shown in Table 2.

Carbonaceous materials

The hydrothermal pretreatment process can facilitate the stabilization of the morphology and structure of the carbon material, thereby enhancing the performance of the battery. This is achieved by introducing a greater number of defects and nanopores, which provide additional active sites for the storage of sodium ions[69]. Lu *et al.* employed a low-cost, high-carbon yield bitumen as a precursor through a pre-oxidation strategy, enabling the bitumen to undergo effective structural transformations from ordered to disordered during the subsequent carbonation process[70]. The structural advantages of disordered carbon help to achieve excellent Na^+ storage performance, resulting in a reversible capacity of 300.6 $mAh·g^{-1}$ at 0.03 $A·g^{-1}$. Zhao *et al.* synthesized an uncommon-performance HC anode with low defects and long-sequence graphite domains of 0.04 m-MnHC by the Mn^{2+} ion-assisted catalytic process, which catalyzed the growth of graphite sheets into long-sequence graphene layers[71]. The SIB anode material had a high ICE (92.05%) and capacity (336.8 $mAh·g^{-1}$ at 0.02 $A·g^{-1}$). Wang *et al.* prepared carbon materials from hazelnut shells by washing with hydrochloric acid to remove impurities and alter microstructure to prepare a HC SIB anode material with a reversible capacity of 342 $mAh·g^{-1}$ at 0.02 $A·g^{-1}$ and an ICE of 91%[72].

Meng *et al.* used the solvothermal method (ST) to form a precursor in liquid phenol-formaldehyde resin (PF) and ethanol (EtOH) with a volume ratio of 2:1, which was carbonized at 1,400 °C, and the synthesized sample was named HC-21-1400[73]. It showed a high reversible capacity of about 410 $mAh·g^{-1}$ and a high ICE of 84% at 0.03 $A·g^{-1}$. The capacity retention was 96% after 40 cycles. Kamiyama *et al.* synthesized the high-capacity HC material HC600-1500 (F50:50) by MgO template technology [Figure 6A][74]. After MgO was removed by pickling, nanoscale pores were formed and these pores were the main active sites for electrochemical sodium storage [Figure 6B and C]. Increasing the pretreatment temperature led to the growth of MgO template particles, resulting in a larger size and number of open micropores. As shown in Figure 6D, HC600-1500 (F50:50) obtained by pickling and post-heating at 1,500 °C showed a high reversible capacity of 478 $mAh·g^{-1}$. It had good capacity retention and excellent ionization rate performance at 0.025 $A·g^{-1}$ [Figure 6E]. Li *et al.* made an HC material from waste cork (CC) as a raw material, which effectively stored sodium ions by adjusting pore types[75]. Due to the natural porous structure of cork, CC presented a uniform layered porous morphology, which improved passivation [Figure 6F and G] (related to platform capacity), and CC-1600 provided a high capacity retention of 87% after 200 cycles at 0.03 $A·g^{-1}$ 0.1 C, with a remaining capacity of 312 $mAh·g^{-1}$ [Figure 6H]. Li *et al.* proposed screening carbon with a highly adjustable nanopore tightened pore inlet, and scalable and reversible low potential platform (< 0.1 V) for high energy anode materials[76]. The results indicated that the constricted pore inlet prevented the formation of a SEI phase within the nanopore, so the Na clusters formed a platform and the number of Na

Table 2. The electrochemical performance of various SIB anode materials after structural regulations

Material	Mechanism	Regulation strategy	ICE (%)	Current density ($mA·g^{-1}$)	Cycles	Capacity retention ($mAh·g^{-1}$)	Ref.
CPOP-1400 °C	Intercalation	Structural	88.6	30	200	281.4	[70]
0.04 m-MnHC	Intercalation	Structural	92.0	20	100	340	[71]
HC-21-1440	Intercalation	Structural	84	60	40	410	[73]
TiO_2(A/B)-MS	Intercalation	Structural	91	2,500	1,000	130	[79]
2D UNs⊂MT@C	Intercalation	Structural	47.1	6,700	5,000	190	[82]
MoO_2/β-MoO_{3-x}	Conversion	Structural	75.9	2,000	500	660	[86]
HCM-Fe_3O_4@void@N-C	Conversion	Structural	62.2	160	800	522	[90]
SFS/C	Conversion	Structural	82.4	5,000	1,000	534.8	[91]
Sb@3D Cu NWAs	Alloying	Structural	64.3	330	200	561.1	[94]
Bulk Bi	Alloying	Structural	97	7,700	3,500	379	[97]

SIB: Sodium-ion battery; ICE: initial coulombic efficiency; TiO_2(A/B)-MS: carbon-free anatase/bronze TiO_2 microspheres; SFS: Sb_2S_3@FeS_2.

clusters increased almost linearly by generating a larger area of hydrophilic pore surface. Moreover, the control of pore diameter ensured the reversibility of sodium cluster formation and generated a screening carbon anode with a superb platform capacity of 400 $mAh·g^{-1}$ at 0.05 $A·g^{-1}$.

Titanium-based oxides

Anatase-type TiO_2 is characterized by an open bilateral TiO_6 octahedral crystal structure, which facilitates the insertion and removal of Na^+. However, weak electronic conductivity and tardy ion diffusion severely limit the remarkable-rate performance of TiO_2. Various strategies have been investigated to modify TiO_2 to enhance Na storage capacity, for instance, the implementation of VO and the designing of nanoscale structures. Ma *et al.* prepared VOs-TiO_{2-x} nanosheets with folds, which increased the conductivity and storage capacity of Na by adding Ti^{3+} and abundant VO[77]. At 20.0 $A·g^{-1}$ the capacity can reach 91.0 $mAh·g^{-1}$ with extremely long cycle stability. Han *et al.* proposed a two-solvent enhanced pressure strategy to prepare N-doped TiO_2/C nanocomposites by using tetrabutyl-n-titanate tetramer as titanium dioxide and reducing its size with mutual solvent ethanol and doped dimethylformamide as pressors[78]. The material had an uncommon specific capacity of 370.4 $mAh·g^{-1}$ at 0.05 $A·g^{-1}$, a superior rate capability of 111.7 $mAh·g^{-1}$ at 17.0 $A·g^{-1}$, and an extensive cycle life of over 20,000 cycles. Hwang *et al.* synthesized carbon-free anatase/bronze TiO_2 microspheres [TiO_2(A/B)-MS] by ST[79]. The highly dense structure constructed by nano-primary particles enhanced the stability of the structure shown in Figure 7A and B. TiO_2(A/B)-MS exhibited a specific capacity of 221 $mAh·g^{-1}$ at 0.025 $A·g^{-1}$ shown in Figure 7C and a superb cycle stability of more than 1,000 cycles at 1.0 and 10.0 C shown in Figure 7D. Yang *et al.* synthesized mesoporous floral titanium-deficient anatase TiO_2 (TDAT)[80]. The presence of Ti vacancies enhanced the conductivity of Li and Na ions and provided additional storage sites. The TDAT electrode had a superb specific capacity of 219.9 $mAh·g^{-1}$ at 0.05 $A·g^{-1}$, excellent rate performance, and brilliant cycle performance of 15,000 cycle tests at 2.0 $A·g^{-1}$.

Lan *et al.* proposed a TiO_2 mesoporous structure with a precisely controlled mesoporous framework[81]. The meticulously crafted mesoscopic TiO_2 model attained a maximum specific capacity of 240 $mAh·g^{-1}$. Under the high mass loading of 9.47 $mg·cm^{-2}$, the area capacity of 2.1 $mAh·cm^{-2}$ was further achieved. Xia *et al.* constructed 2D ultrathin nanosheets (UNs) vertically aligned inside of graphitic carbon-coated mesoporous TiO_2 hollow nanospheres (2D UNs⊂MT@C) shown in Figure 7E[82]. It consisted of regularly alternating monomolecular layers of TiO_2 and carbon, which facilitated rapid electron and Na^+ transportation and abundant 2D heterogeneous interface active sites. The structure demonstrated excellent mechanical stability and structural integrity, ensuring more than 500 cycles at 0.2 C and a capacity decay rate of 0.04% of the battery shown in Figure 7F. At 50 C, the long-term cycle is up to 20,000 times shown in Figure 7G. Liu *et al.*

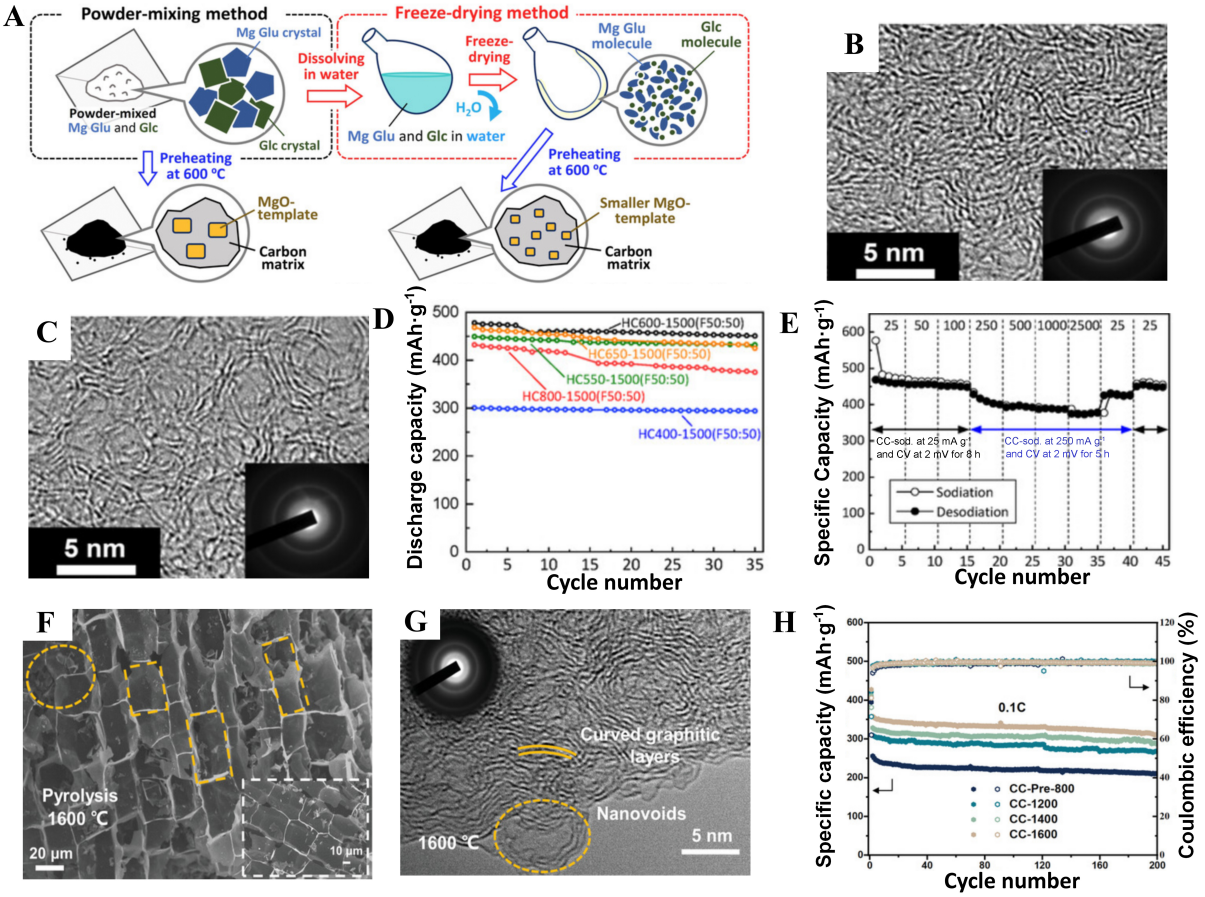

Figure 6. (A) Schematic illustration for the two mixing procedures for preparation of the mixtures of Mg Glu and Glc; TEM images and SAED patterns of (B) HC600-1500 (F0:100) and (C) HC600-1500 (F50:50); (D) Rate performance and (E) Cycle performance of HC600-1500 (F50:50). Quoted with permission from Kamiyama *et al.*[74]; (F) SEM image and (G) HRTEM and SAED images of CC-1600; (H) Cyclic capability of CCs. Quoted with permission from Li *et al.*[75]; Mg Glu: Magnesium gluconate; Glc: glucose; HC600-1500 (F0:100) and HC600-1500 (F50:50): HC by heating the Mg Glu/Glc ratio of 0:100 mol and 50:50 mol, respectively, with preheat-treatment temperature at 600 °C and post-heat-treatment temperatures at 1,500 °C; HC400-1500 (F50:50) and HC550-1500 (F50:50): HC by heating the Mg Glu/Glc ratio of 50:50 mol and preheat-treatment temperature at 400 °C and 550 °C, respectively, with post-heat-treatment temperatures at 1,500 °C; CC-Pre-800: carbonisation process at 800 °C for a period of 2 h, followed by a washing procedure with a dilute hydrochloric acid solution (30% concentration); CC-1200, CC-1400, and CC-1600: cork-derived HC pyrolyzed at 1,200, 1,400, and 1,600 °C, respectively, under argon flow for 2 h; TEM: transmission electron microscopy; SAED: selected area electron diffraction; SEM: scanning electron microscope; HRTEM: high-resolution transmission electron microscopy.

used strong 1D TiO_2 nanowires as a substrate to link these nanosheets together and constructed a bundle layered structure [TiO_2(B)-BH] with a capacity of 131 mAh·g^{-1} at 0.5 C and a distinguished rate of 10 C[83]. A reversible capacity of up to 500 cycles can still be maintained at 85 mAh·g^{-1}.

Conversion-type materials

Yang *et al.* synthesized nickel cobaltite@nitrogen-doped holey graphene (NCO@N-HG) and Fe_3O_4@N-HG composites by loading nickel-cobaltate and magnetite nanoparticles in a 3D nitrogenous porous graphene framework, respectively[84]. The thin graphene sheet buffered volume changes and the unique large pore structure combined with the existence of nanoholes in the graphene sheet facilitated ion transport during the processes of charge/discharge, contributing to the observed superb specific capacity and good cycling performance of 510 mAh·g^{-1} over 100 cycles at 0.1 A·g^{-1}. The ball milling technology[85] was employed to adjust the lattice strain of NiS nanocomposites. The restructured anode had a superb capacity, great rate

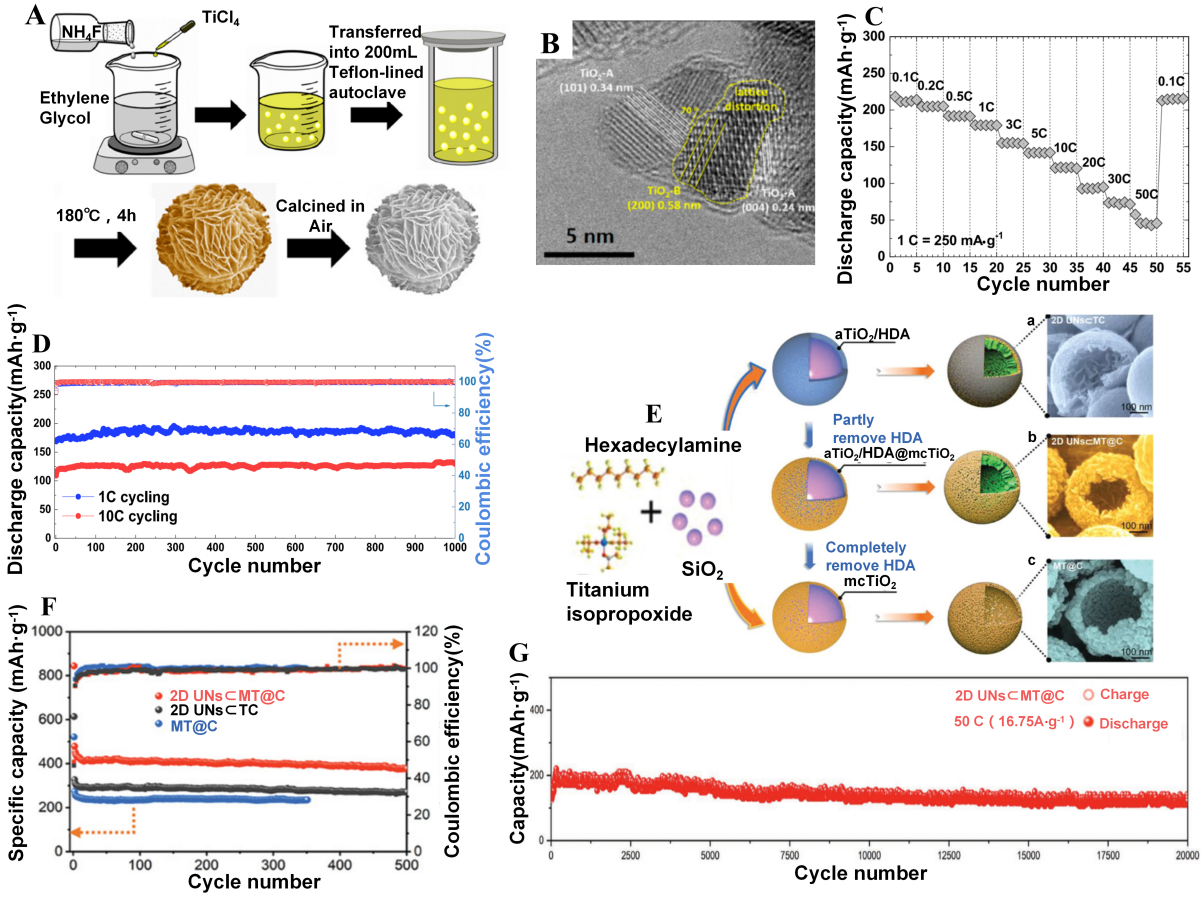

Figure 7. (A) Synthesis process of the TiO_2(A/B)-MS material and its corresponding (B) HRTEM image; (C) Discharge capacities at various C rates; (D) Discharge capacities for long-term cycling. Quoted with permission from Hwang *et al.*[79]; (E) Schematic illustration of the synthesis process of titania-based nanoarchitectures and their corresponding SEM images and (F) Cycling performance at 0.2 C; (G) Long-term cycling performance of 2D UNs⊂TC at 50 C. Quoted with permission from Xia *et al.*[82]. $aTiO_2$/HDA: The titania oligomers by hydrogen-bonding to condense into a compact amorphous inorganic-organic shell; $aTiO_2$/HDA@$mcTiO_2$: a hybrid shell consisting of an amorphous inorganic-organic inner shell tightly confined by a mesoporous crystalline outer shell; $mcTiO_2$: the HDA was partly removed, and a highly crystalline mesoporous shell; 2D UNs⊂TC: hierarchical nano configurations with the stepwise varying morphologies of 2D UNs vertically encapsulated in TiO_2/carbon hollow nanospheres; MT@C: mesoporous hollow nanospheres consisting of graphitic carbon-coated TiO_2 nanocrystals; HRTEM: high-resolution transmission electron microscopy; SEM: scanning electron microscope.

performance (495.7 and 383.2 mAh·g^{-1} at 0.2 and 15.0 A·g^{-1}), and cycle performance (16,000 cycles at 5.0 A·g^{-1}). Li *et al.* successfully prepared micron-scale MoO_2/β-MoO_{3-x} Mosaic composites by *in-situ* micro-corrosion method[86]. Owning to the micron-scale particle morphology, the composite with high solid density (1.68 g·cm^{-3}) and low surface area (8.4 m^2·g^{-1}) exhibited a prominent specific capacity of 1,742 mAh·g^{-1}. Furthermore, the dual conductive design achieved by combining high electrical conductivity MoO_2 and superb ionic conductivity β-MoO_{3-x} resulted in long cycle stability for the micron-sized particles (87% capacity retention after 500 cycles) and impressive rate performance (440 mAh·g^{-1} at 7.0 A·g^{-1}). Wang *et al.* successfully developed a coral-like structure composed of Mn_3O_4 nanotubes embedded in 2D porous graphene sheets using a double template of NaCl and SiO_2[87]. Mn_3O_4@pGS exhibited a prominent specific capacity of 770 mAh·g^{-1} at 0.1 A·g^{-1} for Na^+ storage.

Zhang *et al.* constructed MO@NCF (MO = Co_3O_4, Mn_3O_4, Fe_3O_4, NCF: nitrogen-enriched 3D carbon nanofiber networks) by coordinating nanofibrous carboxymethyl chitosan (CMCh) hydrogel with metal ions to create a steady metal-polysaccharide skeleton, then a multistage porous structure was formed through the pyrolysis process[88]. The Co_3O_4@NCF exhibited an impressive Na^+ storage capacity of 645 mAh·g^{-1} at 0.1 A·g^{-1} and a great rate performance of 191 mAh·g^{-1} at 4.0 A·g^{-1}. Xu *et al.* synthesized R-Co_3O_4/C hybrid hollow spheres composed of Co_3O_4 nanoparticles uniformly dispersed in a carbon matrix[89]. The R-Co_3O_4/C mixed hollow microspheres showed superior Na^+ storage capacity (up to 712 mAh·g^{-1}), remarkable rate capacity (223 mAh·g^{-1} at 5.0 A·g^{-1}), and excellent cycle life (74.5% capacity retention after 500 cycles). Zhao *et al.* prepared highly crystalline mesoporous Fe_3O_4 nanoparticles encapsulated in hollow nitrogenous carbon nanospheres (represented by HCM-Fe_3O_4@void@N-C)[90]. A remarkable specific capacity of 372 mAh·g^{-1} was achieved after the first 5 cycles at 0.16 A·g^{-1}, which can be gradually increased and maintained at 522 mAh·g^{-1} over 800 cycles. In addition, brilliant rate performance of 196 mAh·g^{-1} and high coulomb efficiency (≈ 100%) at 12.0 A·g^{-1} were obtained.

Cao *et al.* successfully fabricated fine hierarchical heterostructures composed of antimonous sulfide Sb_2S_3 @FeS_2 (SFS) hollow nanorods embedded in an N-doped carbon matrix shown in Figure 8A and B[91]. The well-designed architecture facilitated the rapid diffusion of Na ions and enhanced charge transfer at heterogeneous interfaces. Simultaneously, this structure greatly accelerated electron/ion transport and inhibited volume expansion over a long cycle. Thus, the composite demonstrated outstanding rate performance of 537.9 mAh·g^{-1} at 10.0 A·g^{-1} and exceptional cyclic stability of 85.7% capacity retention after 1,000 cycles at 5.0 A·g^{-1} shown in Figure 8C. Liu *et al.* investigated a general strategy for successfully preparing a variety of high entropy oxide-polyoxometalate (HEO-POM) self-assembled nanowires using POM clusters shown in Figure 8D, where the types of metal oxides and POM clusters can be flexibly adjusted[92]. A series of experiments and molecular dynamics simulations showed that the formation of HEO-POM sub-1 nm nanowires (SNWs) followed the oriented attachment mechanism; namely, the POM clusters acted as linkers for multiple metal oxides under the action of van der Waals interactions. CoZnCuNiFeZrCeO_x-phosphomolybdic acid (PMA) SNWs can maintain a high capacity retention of about 92% even after 5,000 cycles at 10 C shown in Figure 8E.

Alloying-type materials

Yang *et al.* designed an optimized Bi@Void@C nanosphere (Bi@Void@C-2) with a yolk-shell structure, which exhibited a conspicuous cycle life of 198 mAh·g^{-1} after 10,000 cycles at 20.0 A·g^{-1}[93]. Theoretical calculations and experimental studies showed that the external layer of the thin carbon shell was of significant importance in improving electronic conductivity and preventing the aggregation of Bi nanoparticles. Fan *et al.* designed a distinctive 3D collector assembled from an array of 1D nanowires (1D NWAs) anchored to 3D porous copper foam for constructing core-shell Cu@Sb nanowires[94]. The resulting 3D hierarchical anode with interconnected 3D micron-sized holes and abundant interwire spaces effectively relieved the structural stress during cycling, which ensured the structural integrity and helped to achieve a uniform ion/electron distribution over the entire surface as shown in Figure 9A. The electrode exhibited a high specific capacity of 605.3 mAh·g^{-1} at 0.33 A·g^{-1} [Figure 9B], and a supernormal capacity retention of 84.8% even at a prominent specific current of 3.3 A·g^{-1} [Figure 9C].

Carbon fiber has excellent electrical conductivity, a significant specific surface area, and superb electrochemical stability. Through electrostatic spinning and reduction roasting, an independent carbon fiber film was obtained. Owing to the superb specific surface area and porosity, the one-dimensional structure provided more active centers and greatly alleviated the volume expansion. Dang *et al.* developed a distinctive pod-like independent film[95]. This film incorporated SbSn particles into an integrated carbon matrix. In addition, the following materials are included: hollow carbon spheres and N-doped carbon fibers

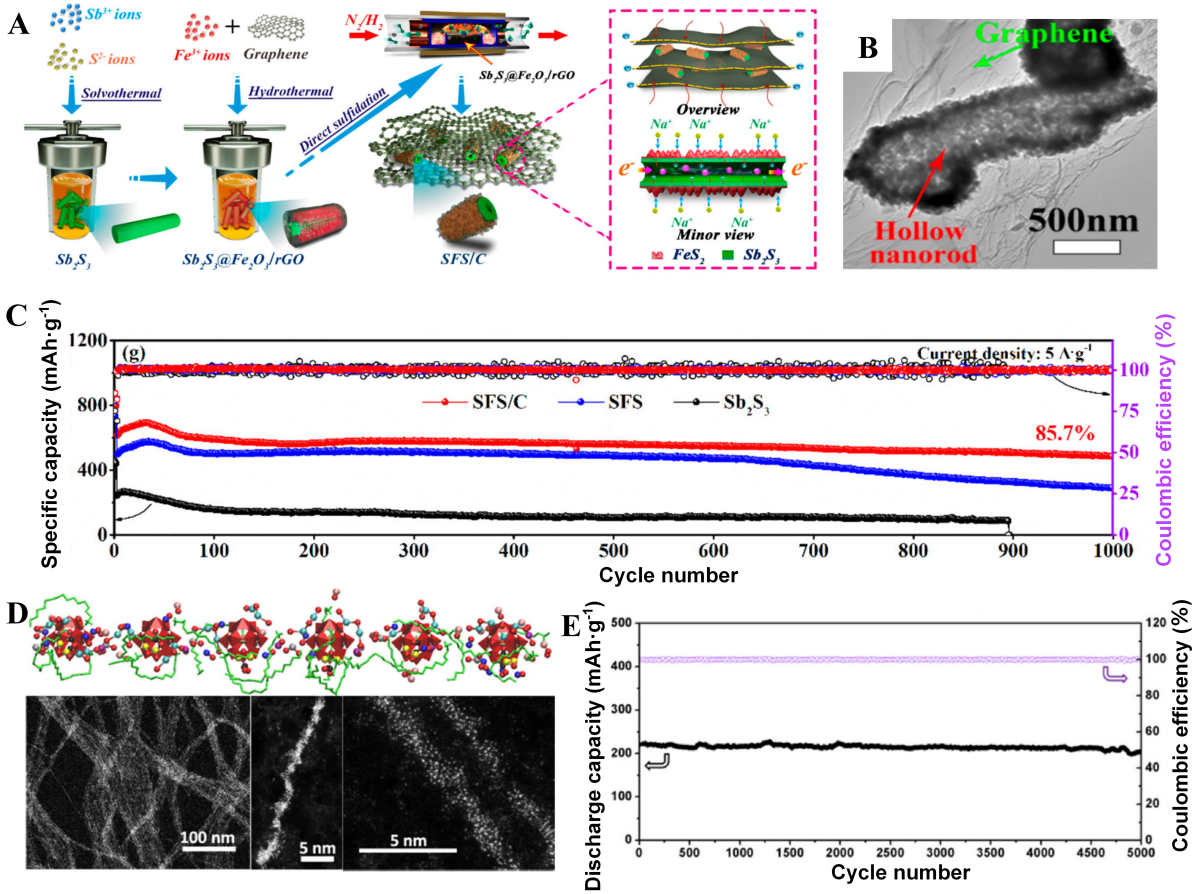

Figure 8. (A) Schematic illustration of the fabrication process of tSFS/C composite and its corresponding (B) TEM image; (C) Cycle performance of SFS/C, SFS, and Sb_2S_3 at 5 A g^{-1}. Quoted with permission from Cao *et al.*[91]; (D) The snapshot of a nanowire composed of $CoZnCuNiFeZrCeO_x$-PMA building blocks with HAADF-STEM images and AC-TEM images; (E) Cycling stability of $CoZnCuNiFeZrCeO_x$-PMA SNWs. Quoted with permission from Liu *et al.*[92]. SFS/C: Sb_2S_3@FeS_2/N-doped graphene; TEM: transmission electron microscopy; PMA: phosphomolybdic acid; HAADF: high-angle annular dark field; STEM: scanning transmission electron microscopy; AC-TEM: aberration-corrected transmission electron microscopy; SNWs: sub-1 nm nanowires.

(B-SbSn/NCFs), which not only improved the electrical conductivity and flexibility but also provided sufficient space to accommodate volume changes. Moreover, the B-SbSn/NCFs self-supporting film can serve as a direct anode without the need for polymer binders and conductors, which improves the energy density and reaction kinetics. The membrane electrode demonstrated a specific capacity of 486.9 mAh·g^{-1} with a coulombic efficiency approaching 100% after 400 cycles at 0.1 A·g^{-1}.

Song *et al.* prepared dispersed *in situ* 3D cross-linked carbon nanofiber SnSb@CNF[96]. The 3D cross-linked nanostructures ensured more Na storage active sites, stable structure, and increased electrical conductivity. Thus, the SnSb@CNF/CNT anode exhibited excellent cycle stability (161 mAh·g^{-1} in 1,000 cycles at 1.0 A·g^{-1}). Kim *et al.* designed a massive bismuth anode that featured ultra-fast charging, long cycle stability, and substantial energy storage capacity without expensive nanomaterials or surface modifications[97]. During the electrolyte cycle of dimethoxy-ethane (DME), the massive Bi particles gradually transformed into porous nanostructures shown in Figure 9D, thus storing Na^+ by forming a phase with high Na diffusivity. Even at the very fast charging rates of 80 and 100 C, 94% and 93% of the capacity measured at 1 C were retained, respectively shown in Figure 9E. The Na-Bi half-cell delivered a specific capacity of 379 mAh·g^{-1} (97% of 1 C measurement) at 7.7 A·g^{-1} (20 C) over 3,500 cycles shown in Figure 9F. Eaves-Rathert *et al.*

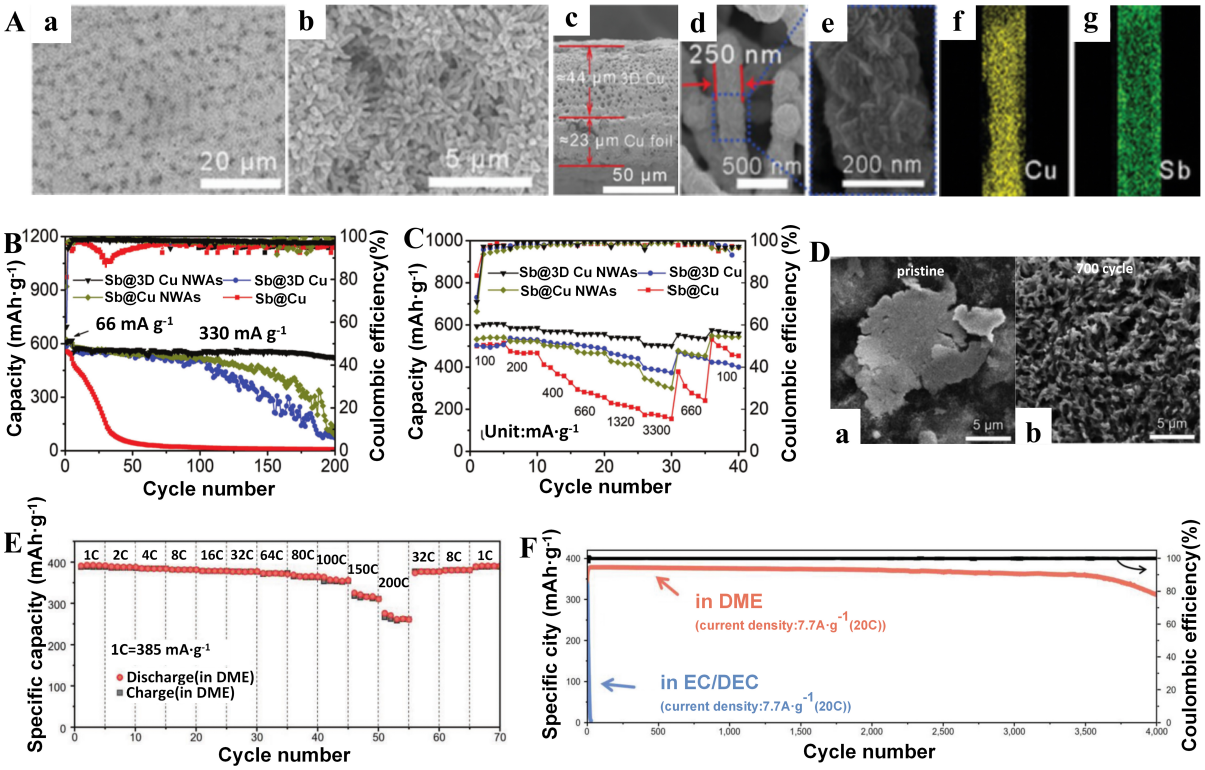

Figure 9. (A) SEM images of Sb@3D Cu NWAs from (a and b) a top view, (c) a side view, and (d and e) an enlarged top view. Energy dispersive X-ray spectroscopy maps for elements (f) Cu and (g) Sb; (B) Cyclability curves; (C) Rate performance. Quoted with permission from Fan *et al.*[94]; (D) Structural evolution of bulk Bi flakes. Secondary-electron images recorded at low magnification; (E) Changes in specific capacity of Na-Bi half-cells measured at various C-rates using an electrolyte containing DME; (F) Changes in the specific capacity of the Na-Bi half-cell with DME and EC/DEC solvent measured at 20.0 C as a function of the battery cycle. Quoted with permission from Kim *et al.*[97]. SEM: Scanning electron microscope; Sb@3D Cu NWAs: a thin film of Sb is electrochemically deposited on 3D Cu NWAs; DME: dimethoxy-ethane; EC: ethylene carbonate; DEC: diethyl carbonate.

designed the microstructured Pb-Sb-Sn, demonstrating that these can be effectively controlled through simple heat treatment of the unrefined powder to achieve a max specific capacity of 522 mAh·g^{-1}[98].

INTERFACIAL REGULATIONS

In a typical SIB system, ICE is utilized to evaluate the reversible migration of Na^+ during the initial charge/discharge process, manifested as the reversible capacity in the first cycle, which is one of the key parameters of SIBs. For a half-cell, the sodium metal can supply excessive Na^+ for sodiation/desodiation, making ICE not crucial. However, in a full-cell, insufficient ICE may result in limited consumption of Na at the cathode, resulting in a decrease in energy density. Therefore, improving the ICE of the anode contributes to promoting the advancement and practical implementation of SIBs significantly. The low ICE is a common problem that exists in all types of SIB anode materials, which is believed to be owe to the irreversible capture of Na^+ and the formation of SEI layers. The structure and morphology of anode materials, such as defects, pores, and crystalline phases, can significantly influence the ICE. Strategies such as modification of the electrode material (doping, surface coating, microstructure, and porosity adjustment to reduce the side reactions of the electrode with the electrolyte) and optimization of the electrolyte composition (salts, solvents, and additives) are beneficial for the construction of an improved SEI and thus improve the ICE[29,31,34,35]. The electrochemical performance of various SIB anode materials after interfacial regulations is shown in Table 3.

Table 3. The electrochemical performance of various SIB anode materials after interfacial regulation

Material	Mechanism	Regulation strategy	ICE (%)	Current density (mA·g^{-1})	Cycles	Capacity retention (mAh·g^{-1})	Ref.
pHC	Intercalation	Interfacial	99.2	50	300	108.9	[99]
H-NTO	Intercalation	Interfacial	49	100	3,000	120	[104]
Li-TiO_2NTS	Intercalation	Interfacial	87	1,000	250	132	[106]
Sn-MnO@C	Conversion	Interfacial	91.5	1,000	500	214	[107]
Sn@NC	Alloying	Interfacial	78.4	1,000	400	474	[108]

SIB: Sodium-ion battery; ICE: initial coulombic efficiency; pHC: presodiated HC; H-NTO: hollow $Na_2Ti_3O_7$.

Carbonaceous materials

HC has a substantial specific surface area and numerous defect sites and more sodium ions need to be sacrificed to form SEI films, which ultimately generates an increase in irreversible specific capacity and a decrease in coulombic efficiency. The ICE of graphite anode is more than 90% while that of HC anode is usually only 60% to 80%.

Fang *et al.* employed sodium diphenyl ketone (Na-DK) as a reducing agent for the bifunctional preparation of HC[99]. The chemically synthesized sodium facilitated the formation of a robust sodium fluoride (NaF)-rich SEI layer in the electrolyte by pre-doping HC. Figure 10A analyzes the optimal structure of adsorbed and non-adsorbed Na^+, revealing the interaction of Na^+, dibenzoyl (DK), and HC. As illustrated in Figure 10B, the presodiated HC (pHC) anode exhibited a high reversible capacity of 251.5 mAh·g^{-1} at 0.5 A·g^{-1}. As demonstrated in Figure 10C, it enabled a full battery of pHC//$Na_3V_2(PO_4)_3$ (NVP) to operate for over 700 cycles with minimal capacity degradation. Bai *et al.* developed a sustainable film for an SEI on an HC anode by adding a small amount of ester additive as an agent for forming the SEI film in the ether-based electrolyte is illustrated in Figure 10D[100]. This membrane prevented the coupling of the protective SEI with the fast transmission of Na^+, leading to improved electrochemical performance of the HC anode and effectively shielding the HC electrode from the influence of structural changes shown in Figure 10E and F. The material had a specific capacity of 211 mAh·g^{-1} after 2,000 cycles at 1.0 A·g^{-1}. The decay rate was only 0.0023% per cycle displayed in Figure 10G.

Jin *et al.* presented an advanced electrolyte containing sodium difluorosulfonyl imide (NaFSI)-triethyl phosphate (TEP), which exhibited great stability with high voltage cathodes and was able to improve the cycling of Na^+ batteries[101]. The Na||$NaNi_{0.68}Mn_{0.22}Co_{0.10}O_2$ (NaNMC) battery demonstrated a capacity retention of 89% after 500 cycles with a cut-off voltage of 4.2V (*vs.* Na^+/Na). Jin *et al.* introduced NaFSI-TEP/1,1,2,2-tetrafluoroethyl-2,2,3,3-tetrafluoropropyl ether (TTE) (molar ratio 1:1.5:2), a non-combustible electrolyte for SIBs, which stabilized the interface at the layered O_3-$NaCu_{1/9}Ni_{2/9}Fe_{1/3}Mn_{1/3}O_2$ (Na-CNFM) cathode and HC anode simultaneously for consistent cyclic performance[102]. The capacity retention rate of Na||HC battery after 500 cycles was 94.8% (247.9 mAh·g^{-1}). The high-quality interface established on both the cathode and anode ensured HC's exceptional cycle stability.

Titanium-based oxides

Li *et al.* combined 16 nm anatase TiO_2 with diglyme-based electrolyte and the reversible capacity reached 257.9 and over 100 mAh·g^{-1} at 0.1 and 2.0 A·g^{-1}[103]. Both of them were significantly better than the ethylene carbonate (EC)/diethyl carbonate (DEC)-based electrolytes. It had been shown that the ether-based electrolyte promoted the Na^+-induced TiO_2 structure transformation, and the charge transfer kinetics at the SEI/electrode interface played a crucial role in rate cycling performance. Meng *et al.* reported hollow NTO microspheres (H-NTO) with oxygen defects prepared from 2D ultra-thin nanosheets[104]. These microspheres exhibited a unique chemical bonding NTO/C(N) interface shown in Figure 11A. When the

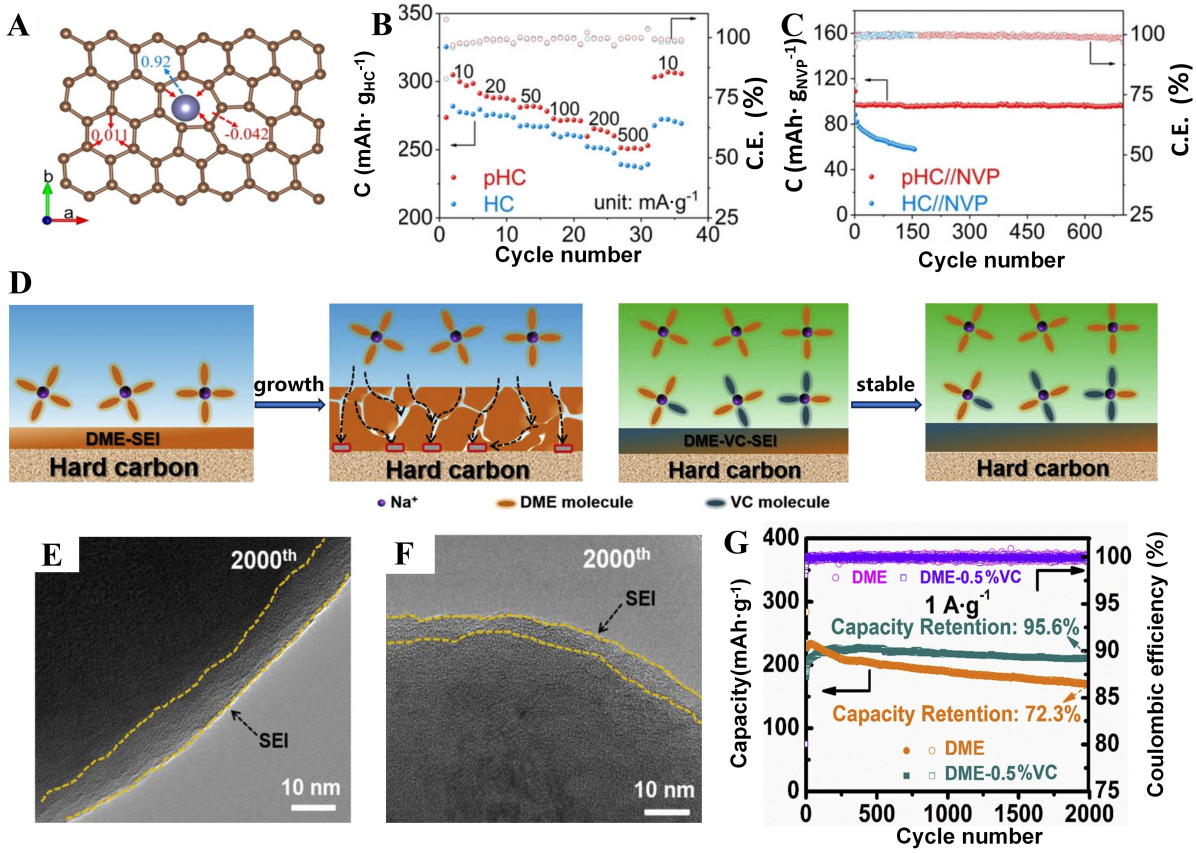

Figure 10. (A) Optimized structures of Na^+ adsorbed on graphene layer of 60 carbon atoms containing five/seven-membered rings; (B) Rate capability of HC and pHC; (C) Cycle performance of full cells at 0.5 A·g^{-1} of pHC//NVP and HC//NVP. Quoted with permission from Fang *et al.*[99]; (D) Schematic illustration of the evolution of SEI films in the DME-based and DME-0.5%VC electrolytes upon prolonged cycling on HCs; TEM images of HC anodes after 2,000 cycles in the (E) DME-based and (F) DME-0.5%VC electrolytes; (G) Long-term cycling performance. Quoted with permission from Bai *et al.*[100]. DME-VC-SEI: SEI films in DME and vinylene carbonate electrolytes; HC: hard carbon; pHC: presodiated HC; NVP: $Na_3V_2(PO_4)_3$; SEI: solid electrolyte interphase; DME: dimethoxy-ethane; TEM: transmission electron microscopy.

temperature reached 60 °C, the specific capacity of the H-NTO electrode was 59 mAh·g^{-1} at 20 A·g^{-1} demonstrated in Figure 11B. By optimizing the electrolyte, the H-NTO electrode can be stably cycled at -40 °C for 200 days without a decrease in capacity shown in Figure 11C. The outstanding cycling stability was due to the stable SEI formed by the NTO/C(N) interface and the highly adaptable electrolyte/electrode interface.

Xu *et al.* showed that anatase TiO_2 underwent amorphous crystallization during the first alkalization process and in the subsequent cycles[105]. The amorphous phase showed pseudo-capacitor sodium storage behavior. For the first time, it was found that the ether-based electrolyte was able to form a thin (≈ 2.5 nm) and stable SEI layer while the conventional carbonate-based electrolyte could form a thick (≈ 10 nm) and growing SEI layer. The elevated minimum molecular orbital energy of the ether solvent/ionic complexes was the underlying cause of this discrepancy. In the ether-based electrolyte, after 500 cycles, a specific capacity of 192 mAh·g^{-1} can be achieved at 0.1 A·g^{-1}, which significantly exceeds the capacity of the carbonate electrolyte. Cha *et al.* obtained significantly enhanced SEI layers on TiO_2 nanotube (TiO_2 NTS) arrays, which improved the performance of sodium battery systems[106]. Pre-insertion of Li^+ into TiO_2NTS can make SEI meet the conditions of Na^+ replacement shown in Figure 11D. SIBs constructed using pre-embedded

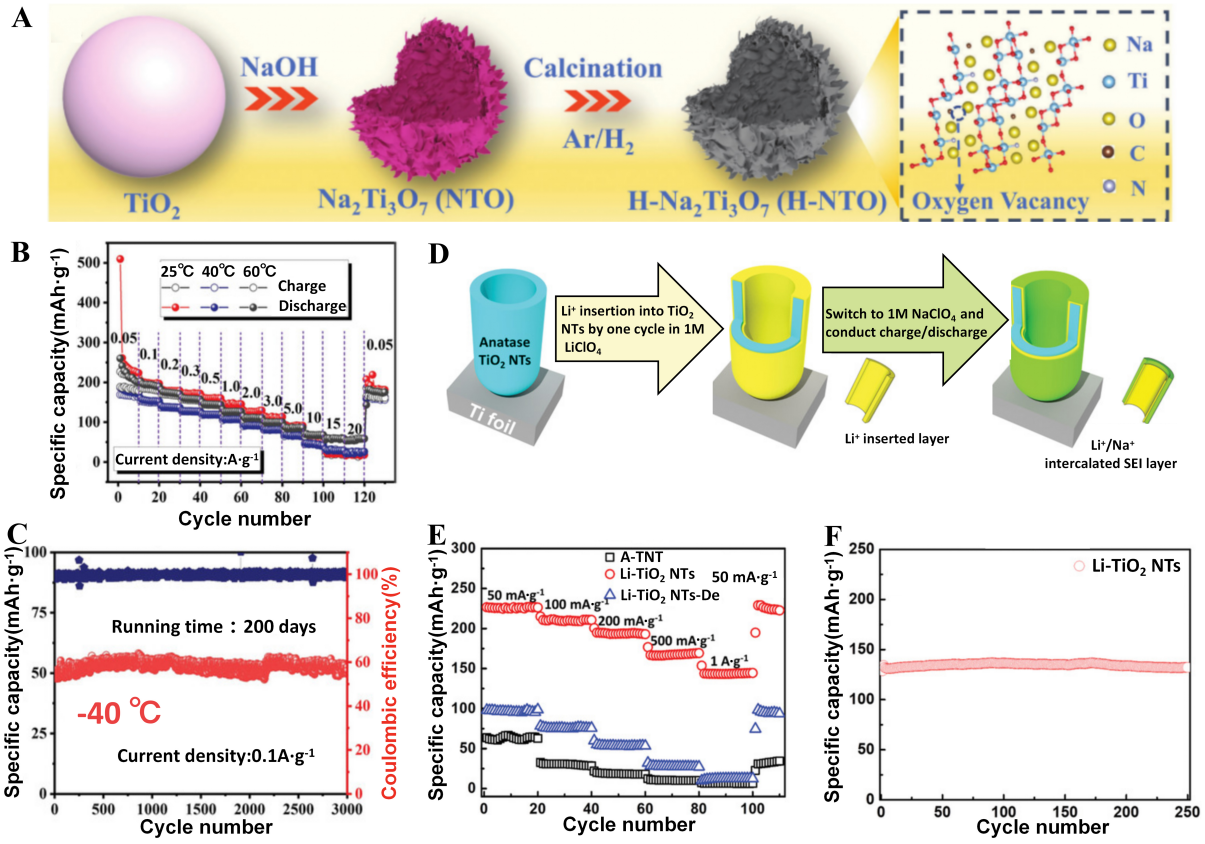

Figure 11. (A) Synthetic route for H-NTO microspheres and its corresponding (B) Rate performance at different temperatures; (C) Cycle performance. Quoted with permission from Meng *et al.*[104]; (D) Synthesis of Li^+ pre-inserted SEI layer; (E) Rate performance; (F) Cycling performance at 1.0 $A·g^{-1}$. Quoted with permission from Cha *et al.*[106]. A-TNT: Anatase TiO_2 NTs (A-TNT); Li-TiO_2 NTs: Li^+ inserted anatase TiO_2 NTs; Li-TiO_2 NTs-De: Li^+ inserted/de-inserted anatase TiO_2 NTs; H-NTO: hollow $Na_2Ti_3O_7$; SEI: solid electrolyte interphase.

lithium nanotubes had superb rate capability (132 $mAh·g^{-1}$ at 1.0 $A·g^{-1}$) shown in Figure 11E and superb Na^+ cycle stability (capacity retention of 99.9% after 250 cycles at 1.0 $A·g^{-1}$) shown in Figure 11F.

Conversion-type and alloying-type materials

Li *et al.* developed a new novel type of alloying/conversion-based anode in which the metal oxide (e.g., MnO) micro dumbbell skeleton was designed to stabilize large capacity alloyed (e.g., Sn) nanoparticles[107]. In combination with electrolyte engineering methods, the Sn-MnO@C anode exhibited outstanding Na^+ storage performance, including an excellent specific capacity of 370 $mAh·g^{-1}$, a good rate capacity of more than 10 $A·g^{-1}$, and a favorable cycling life of more than 500 cycles. Yang *et al.* performed surface engineering on tin nanorods by using N-doped carbon layers (Sn@NC) and interface engineering strategy shown in Figure 12A[108]. The uniform surface modification effectively enhanced electron and Na^+ transport kinetics and interacted with the ether-based electrolyte to form a strong organic-inorganic SEI shown in Figure 12B. Moreover, Sn@NC anodes provided ultra-long cycle stability of more than 10,000 cycles shown in Figure 12C.

Chu *et al.* employed an ultra-low concentration electrolyte strategy that included a significantly high amount of sodium salts of tetra phenyl-borate ion (BPH^{4-}) and a DME solvent to stabilize micron tin and bismuth anodes[109]. In the 0.1 M $NaBPh_4$-DME electrolyte, sodium had a faster migration rate attributed to

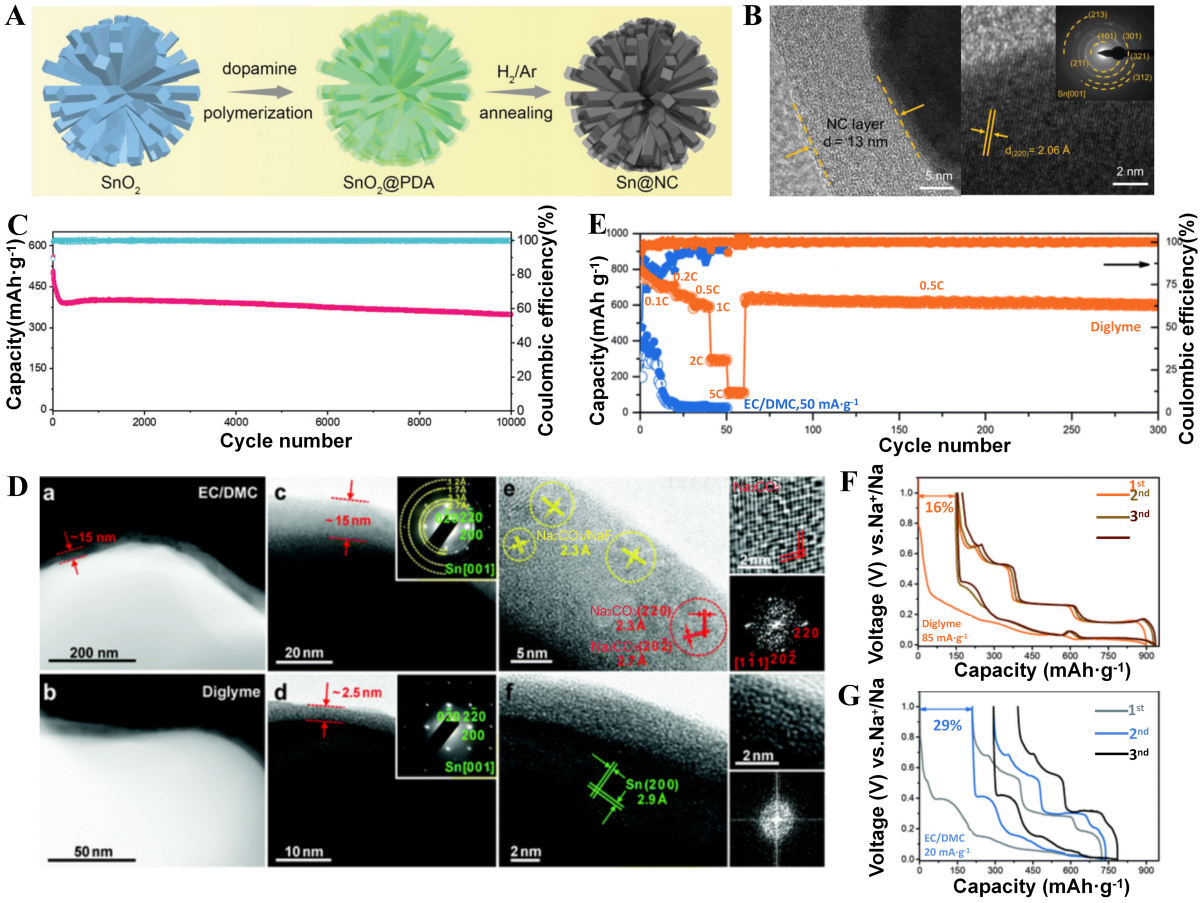

Figure 12. (A) Schematic of synthesis of Sn@NC composite and its (B) TEM image; (C) Long cycling performance of composite anodes at 5.0 $A·g^{-1}$ in the DEGDME-based electrolyte. Quoted with permission from Yang *et al.*[108]; (D) Composition/nanostructure of SEIs probed by cryo-TEM and XPS. (a-f) HAADF STEM and TEM images of SEIs in (a, c, and e) $NaBF_4$/EC/DMC and (b, d and f) $NaBF_4$/diglyme with SAED as insets in (c and d). Note that the insets in (e and f) are the enlarged HRTEM and FFT images for the SEI layer region; (E) Cyclic stability of Sn microparticle electrodes; (F and G) The first three discharge/charge curves. Quoted with permission from Huang *et al.*[110]. SnO_2@PDA: The SnO_2 nanorods were further encapsulated by dopamine; Sn@NC: 3D flower-like architecture consisting of nitrogen-doped carbon-coated tin nanorods; TEM: transmission electron microscopy; DEGDME: diethylene glycol dimethyl ether; SEIs: solid electrolyte interphases; XPS: X-ray photoelectron spectroscopy; HAADF: high-angle annular dark field; STEM: scanning transmission electron microscopy; TEM: transmission electron microscopy; EC: ethylene carbonate; DMC: dimethyl carbonate; SAED: selected area electron diffraction; HRTEM: high-resolution transmission electron microscopy; FFT: fast Fourier transform.

the significant steric hindrance of BPH^{4-} anion, which made it difficult to approach the electrode/electrolyte interface and thus the side reactions at the electrode/electrolyte interface were reduced. With electrolyte optimization, the specific capacity of 600 $mAh·g^{-1}$ on the Sn anode can be reached at 0.5 $A·g^{-1}$. Huang *et al.* explored the nanostructure and nanomechanical SEI derived from carbonate-and ether-based materials on micron-sized tin particles[110]. The structure/composition and properties of SEI derived from EC/DMC and diethylene glycol dimethyl ether were elucidated. The SEI derived from diethylene glycol dimethyl ether exhibited high elasticity and ionic conductivity, which can be attributed to the unique structure of the amorphous particles dispersed in polymer-like substances shown in Figure 12D. Compared to the $NaBF_4$/(EC/DMC) electrolytic liquid phase, the diethylene glycol electrolyte provided significantly improved coulomb efficiency and cycle stability shown in Figure 12E-G.

Wu *et al.* demonstrated the rapid production of ultrafine Bi nanoparticles embedded in a 3D carbon framework (Bi@3D-CF) by a Joule heating method with a synthesis time of just 30 s[111]. The Bi@3D-CF exhibited excellent Na storage performance in 1,2-DME based electrolyte with a capacity of 349 $mAh \cdot g^{-1}$ after 12,000 cycles at 5.0 $A \cdot g^{-1}$, and 311 $mAh \cdot g^{-1}$ at 100 $A \cdot g^{-1}$. The outstanding performance was attributed to the formation of unique 3D porous structures during cycling and the gradient organic/inorganic SEI.

CONCLUSION AND OUTLOOKS

In this review, we have summarized various synthesis and regulation strategies, such as composition regulation (heteroatom doping, composite construction, and formation of heterostructure), structural regulation (nanostructure design, morphology control, and defect introduction), and interfacial regulation (the regulation of electrode materials and electrolyte salts, solvents, and additives to form a stable SEI) to improve the electrochemical performance of intercalation-type, conversion-type, and alloying-type SIB anode materials with selected examples. The underlying mechanism is to provide more storage/active cites, reduce the strain stress, improve the electronic/ionic conductivity of the electrode materials, and suppress/reduce the electrolyte decomposition by composition and structure modulation to improve their specific capacity, cycling stability, and rate capability. Here are the conclusions and outlooks:

(1) Heteroatom doping, composite construction, and defect introduction are the most critical strategies for intercalation-type SIB anode materials to improve the specific capacity and rate capability. Formation of heterostructure, nanostructure design, and morphology control are the most vital strategies for conversion-type and alloying-type SIB anode materials to improve cycling stability and rate capability. Interfacial regulation strategies are highly desired for each type of SIB anode material because low ICE is the common challenge that all three types of anode materials have to face. By comparing the ideal electrochemical performance of SIB anode materials afore-mentioned in the introduction with the obtained electrochemical performance of various anode materials listed in Tables 1-3, it is evident that despite the implementation of diverse synthesis and regulation strategies, the above-mentioned various SIB anode materials only partially meet the application requirements. Among them, HC is the most appealing anode material for the commercialization of SIBs as it shows the best sodium ion storage performance and is widely available, affordable, and environmentally friendly. Especially, the specific capacity of HC has reached 300 $mAh \cdot g^{-1}$ and the electrical conductivity can also be improved through N, O, S, and other heteroatom doping. However, the overall performance is still not satisfactory; the specific capacity and rate capability need to be further improved, especially the long-term cycle stability and the low ICE needs to be improved as well. Titanium-based oxides have excellent cycling stability while their specific capacities and ICE still need to be further improved. The conversion type material has a theoretical specific capacity ranging from 800 to 1,200 $mAh \cdot g^{-1}$ and the alloying material containing P can reach 2,569 $mAh \cdot g^{-1}$. However, there is a significant volume change during the charge/discharge process of these materials, which is far more than 20% of the commercial standard.

(2) Beyond the mainstream intercalation, conversion, and alloying-type anode materials, metal-organic frameworks (MOFs)[112-115], covalent organic frameworks (COFs)[116,117], and organic materials[118-120] have become one of the important classes of materials for SIB anodes in recent years. MOFs are generated by the self-assembly of metal nodes and organic ligands via coordination bonds. They possess high specific surface areas and tunable pore structures, which enable MOFs to provide abundant active sites and favorable ion diffusion channels, thus improving the specific capacity and rate capability used as SIB anodes. COFs are crystalline porous materials formed by connecting organic units through covalent bonds. They exhibit resource sustainability, structural designability, and excellent chemical stability, which enable COFs to provide designable and stable structures, thus improving the selectivity and cycling stability used as SIB

anodes. Similar to COFs, resource sustainability and structural designability allow organic materials to optimize their sodium-ion storage performance accordingly and flexibly. Thus, the sustainability, versatility, and customizability of MOFs, COFs, and organics allow them to show great prospects for the development of next-generation high-performance SIB anode materials. With ongoing advancements in materials science and electrochemical engineering, the performance of these materials is expected to be further enhanced, promoting the SIB technique toward commercialization.

(3) In this review, we mainly discussed the improvement of the sodium ion storage performance of anodes from the materials design aspect. Nevertheless, for plenty of sodiation/desodiation processes, the related structure-performance relationships and the underlying reaction mechanisms are still unclear. This can be effectively solved by the application of *in situ*/operando characterization techniques such as Raman/infrared (IR) spectroscopy, X-ray diffraction (XRD), and transmission electron microscopy (TEM) to monitor the reaction processes. The obtained information can elucidate the structure-performance relationships and the underlying reactions, guiding the rational design of SIB anode materials with superior performance.

DECLARATIONS

Authors' contributions

Wrote the draft manuscript: Lin, Y. T.; Lin, B. L.; Niu, B. T.; Lin, X. M.
Revised the manuscript: Chen, X. P.; Guo, H. X.; Lin, X. M.
Guided this work: Lin, X. M.

Availability of data and materials

Not applicable.

Financial support and sponsorship

We are grateful to the National Natural Science Foundation of China (22272069) and the Natural Science Foundation of Fujian Province (2021J01988 and 2022J05173).

Conflicts of interest

All authors declared that there are no conflicts of interest.

Ethical approval and consent to participate

Not applicable.

Consent for publication

Not applicable.

REFERENCES

1. Li, M.; Lu, J.; Chen, Z.; Amine, K. 30 years of lithium-ion batteries. *Adv. Mater.* **2018**, *30*, e1800561. DOI PubMed
2. Weiss, M.; Ruess, R.; Kasnatscheew, J.; et al. Fast charging of lithium-ion batteries: a review of materials aspects. *Adv. Energy. Mater.* **2021**, *11*, 2101126. DOI
3. Xu, J.; Cai, X.; Cai, S.; et al. High-energy lithium-ion batteries: recent progress and a promising future in applications. *Energy. Environ. Maters.* **2023**, *6*, e12450. DOI
4. Nayak, P. K.; Yang, L.; Brehm, W.; Adelhelm, P. From lithium-ion to sodium-ion batteries: advantages, challenges, and surprises. *Angew. Chem. Int. Ed. Engl.* **2018**, *57*, 102-20. DOI PubMed
5. Chayambuka, K.; Mulder, G.; Danilov, D. L.; Notten, P. H. L. From Li-ion batteries toward Na-ion chemistries: challenges and

opportunities. *Adv. Energy. Mater.* **2020**, *10*, 2001310. DOI

6. Huang, Y.; Zhao, L.; Li, L.; Xie, M.; Wu, F.; Chen, R. Electrolytes and electrolyte/electrode interfaces in sodium-ion batteries: from scientific research to practical application. *Adv. Mater.* **2019**, *31*, e1808393. DOI PubMed
7. Qiao, S.; Zhou, Q.; Ma, M.; Liu, H. K.; Dou, S. X.; Chong, S. Advanced anode materials for rechargeable sodium-ion batteries. *ACS. Nano.* **2023**, *17*, 11220-52. DOI PubMed
8. Chen, J.; Adit, G.; Li, L.; Zhang, Y.; Chua, D. H. C.; Lee, P. S. Optimization strategies toward functional sodium-ion batteries. *Energy. Environ. Mater.* **2023**, *6*, e12633. DOI
9. Chen, X.; Yin, X.; Aslam, J.; Sun, W.; Wang, Y. Recent progress and design principles for rechargeable lithium organic batteries. *Electrochem. Energy. Rev.* **2022**, *5*, 135. DOI
10. Wu, X.; Feng, X.; Yuan, J.; et al. Thiophene functionalized porphyrin complexes as novel bipolar organic cathodes with high energy density and long cycle life. *Energy. Storage. Mater.* **2022**, *46*, 252-8. DOI
11. Yang, G.; Zhu, Y.; Zhao, Q.; et al. Advanced organic electrode materials for aqueous rechargeable batteries. *Sci. China. Chem.* **2024**, *67*, 137-64. DOI
12. Zhang, X.; Xing, P.; Madanu, T. L.; Li, J.; Shu, J.; Su, B. L. Aqueous batteries: from laboratory to market. *Natl. Sci. Rev.* **2023**, *10*, nwad235. DOI PubMed PMC
13. Zhang, H.; Gao, Y.; Liu, X.; et al. Long-cycle-life cathode materials for sodium-ion batteries toward large-scale energy storage systems. *Adv. Energy. Mater.* **2023**, *13*, 2300149. DOI
14. Yao, H.; Zheng, L.; Xin, S.; Guo, Y. Air-stability of sodium-based layered-oxide cathode materials. *Sci. China. Chem.* **2022**, *65*, 1076-87. DOI
15. Ma, Y.; Hu, Y.; Pramudya, Y.; et al. Resolving the role of configurational entropy in improving cycling performance of multicomponent hexacyanoferrate cathodes for sodium-ion batteries. *Adv. Funct. Mater.* **2022**, *32*, 2202372. DOI
16. Hao, Z.; Shi, X.; Yang, Z.; et al. The distance between phosphate-based polyanionic compounds and their practical application for sodium-ion batteries. *Adv. Mater.* **2024**, *36*, e2305135. DOI PubMed
17. Pramanik, A.; Manche, A. G.; Sougrati, M. T.; Chadwick, A. V.; Lightfoot, P.; Armstrong, A. R. $K_2Fe(C_2O_4)_2$: an oxalate cathode for Li/Na-ion batteries exhibiting a combination of multielectron cation and anion redox. *Chem. Mater.* **2023**, *35*, 2600-11. DOI PubMed PMC
18. Lin, X.; Yang, X.; Chen, H.; et al. In situ characterizations of advanced electrode materials for sodium-ion batteries toward high electrochemical performances. *J. Energy. Chem.* **2023**, *76*, 146-64. DOI
19. Chen, X.; Liu, C.; Fang, Y.; et al. Understanding of the sodium storage mechanism in hard carbon anodes. *Carbon. Energy.* **2022**, *4*, 1133-50. DOI
20. Zhao, L.; Hu, Z.; Lai, W.; et al. Hard carbon anodes: fundamental understanding and commercial perspectives for Na-ion batteries beyond Li-ion and K-ion counterparts. *Adv. Energy. Mater.* **2021**, *11*, 2002704. DOI
21. Li, Y.; Lu, Y.; Adelhelm, P.; Titirici, M. M.; Hu, Y. S. Intercalation chemistry of graphite: alkali metal ions and beyond. *Chem. Soc. Rev.* **2019**, *48*, 4655-87. DOI PubMed
22. Peng, P.; Wu, Y.; Li, X.; et al. Toward superior lithium/sodium storage performance: design and construction of novel TiO_2-based anode materials. *Rare. Met.* **2021**, *40*, 3049-75. DOI
23. Dong, J.; Jiang, Y.; Wang, R.; Wei, Q.; An, Q.; Zhang, X. Review and prospects on the low-voltage $Na_2Ti_3O_7$ anode materials for sodium-ion batteries. *J. Energy. Chem.* **2024**, *88*, 446-60. DOI
24. Yang, Z.; Zhang, J.; Kintner-Meyer, M. C.; et al. Electrochemical energy storage for green grid. *Chem. Rev.* **2011**, *111*, 3577-613. DOI PubMed
25. Lin, X.; Chen, J.; Fan, J.; et al. Synthesis and operando sodiation mechanistic study of nitrogen-doped porous carbon coated bimetallic sulfide hollow nanocubes as advanced sodium ion battery anode. *Adv. Energy. Mater.* **2019**, *9*, 1902312. DOI
26. Konkena, B.; Kalapu, C.; Kaur, H.; et al. Cobalt oxide 2D nanosheets formed at a polarized liquid|liquid interface toward high-performance Li-ion and Na-ion battery anodes. *ACS. Appl. Mater. Interfaces.* **2023**, *15*, 58320-32. DOI PubMed PMC
27. Yang, X. T.; Huang, T. Y.; Wang, Y. H.; et al. Understanding the origin of the improved sodium ion storage performance of the transition metal oxide@carbon nanocomposite anodes. *J. Chem. Phys.* **2023**, *158*, 174708. DOI PubMed
28. Wu, Y.; Yao, Y.; Wang, L.; Yu, Y. Recent progress on modification strategies of alloy-based anode materials for alkali-ion batteries. *Chem. Res. Chin. Univ.* **2021**, *37*, 200-9. DOI
29. Wu, X.; Lan, X.; Hu, R.; Yao, Y.; Yu, Y.; Zhu, M. Tin-based anode materials for stable sodium storage: progress and perspective. *Adv. Mater.* **2022**, *34*, e2106895. DOI PubMed
30. Tan, M.; Han, S.; Li, Z.; Cui, H.; Lei, D.; Wang, C. Compact Sn/C composite realizes long-life sodium-ion batteries. *Nano. Res.* **2023**, *16*, 3804-13. DOI
31. Huang, H.; Xu, R.; Feng, Y.; et al. Sodium/potassium-ion batteries: boosting the rate capability and cycle life by combining morphology, defect and structure engineering. *Adv. Mater.* **2020**, *32*, e1904320. DOI PubMed
32. Guo, S.; Yi, J.; Sun, Y.; Zhou, H. Recent advances in titanium-based electrode materials for stationary sodium-ion batteries. *Energy. Environ. Sci.* **2016**, *9*, 2978-3006. DOI
33. Lao, M.; Zhang, Y.; Luo, W.; Yan, Q.; Sun, W.; Dou, S. X. Alloy-based anode materials toward advanced sodium-ion batteries. *Adv. Mater.* **2017**, *29*, 1700622. DOI PubMed
34. Zhang, M.; Li, Y.; Wu, F.; Bai, Y.; Wu, C. Boost sodium-ion batteries to commercialization: strategies to enhance initial coulombic

efficiency of hard carbon anode. *Nano. Energy.* **2021**, *82*, 105738. DOI

35. He, H.; Sun, D.; Tang, Y.; Wang, H.; Shao, M. Understanding and improving the initial Coulombic efficiency of high-capacity anode materials for practical sodium ion batteries. *Energy. Storage. Mater.* **2019**, *23*, 233-51. DOI
36. Li, Y.; Chen, M.; Liu, B.; Zhang, Y.; Liang, X.; Xia, X. Heteroatom doping: an effective way to boost sodium ion storage. *Adv. Energy. Mater.* **2020**, *10*, 2000927. DOI
37. Zhao, R.; Sun, N.; Xu, B. Recent advances in heterostructured carbon materials as anodes for sodium-ion batteries. *Small. Struct.* **2021**, *2*, 2100132. DOI
38. Li, Y.; Wu, F.; Li, Y.; et al. Ether-based electrolytes for sodium ion batteries. *Chem. Soc. Rev.* **2022**, *51*, 4484-536. DOI PubMed
39. Tian, Z.; Zou, Y.; Liu, G.; et al. Electrolyte solvation structure design for sodium ion batteries. *Adv. Sci.* **2022**, *9*, e2201207. DOI PubMed PMC
40. Cheng, H.; Sun, Q.; Li, L.; et al. Emerging era of electrolyte solvation structure and interfacial model in batteries. *ACS. Energy. Lett.* **2022**, *7*, 490-513. DOI
41. Pei, Z.; Meng, Q.; Wei, L.; Fan, J.; Chen, Y.; Zhi, C. Toward efficient and high rate sodium-ion storage: a new insight from dopant-defect interplay in textured carbon anode materials. *Energy. Storage. Mater.* **2020**, *28*, 55-63. DOI
42. Jin, Q.; Wang, K.; Feng, P.; Zhang, Z.; Cheng, S.; Jiang, K. Surface-dominated storage of heteroatoms-doping hard carbon for sodium-ion batteries. *Energy. Storage. Mater.* **2020**, *27*, 43-50. DOI
43. Xie, F.; Niu, Y.; Zhang, Q.; et al. Screening heteroatom configurations for reversible sloping capacity promises high-power Na-ion batteries. *Angew. Chem. Int. Ed. Engl.* **2022**, *61*, e202116394. DOI PubMed
44. Wu, S.; Peng, H.; Xu, J.; et al. Nitrogen/phosphorus co-doped ultramicropores hard carbon spheres for rapid sodium storage. *Carbon* **2024**, *218*, 118756. DOI
45. Mehmood, A.; Ali, G.; Koyutürk, B.; Pampel, J.; Chung, K. Y.; Fellinger, T. Nanoporous nitrogen doped carbons with enhanced capacity for sodium ion battery anodes. *Energy. Storage. Mater.* **2020**, *28*, 101-11. DOI
46. Tao, S.; Xu, W.; Zheng, J.; et al. Soybean roots-derived N, P Co-doped mesoporous hard carbon for boosting sodium and potassium-ion batteries. *Carbon* **2021**, *178*, 233-42. DOI
47. Yan, J.; Li, H.; Wang, K.; et al. Ultrahigh phosphorus doping of carbon for high-rate sodium ion batteries anode. *Adv. Energy. Mater.* **2021**, *11*, 2003911. DOI
48. Fan, M.; Lin, Z.; Zhang, P.; et al. Synergistic effect of nitrogen and sulfur dual-doping endows TiO_2 with exceptional sodium storage performance. *Adv. Energy. Mater.* **2021**, *11*, 2003037. DOI
49. Luo, S.; Yuan, T.; Soule, L.; et al. Enhanced ionic/electronic transport in nano-TiO_2/sheared CNT composite electrode for Na^+ insertion-based hybrid ion-capacitors. *Adv. Funct. Mater.* **2020**, *30*, 1908309. DOI
50. Wang, C.; Zhang, J.; Wang, X.; Lin, C.; Zhao, X. S. Hollow rutile cuboid arrays grown on carbon fiber cloth as a flexible electrode for sodium-ion batteries. *Adv. Funct. Mater.* **2020**, *30*, 2002629. DOI
51. Lv, D.; Wang, D.; Wang, N.; et al. Nitrogen and fluorine co-doped TiO_2/carbon microspheres for advanced anodes in sodium-ion batteries: high volumetric capacity, superior power density and large areal capacity. *J. Energy. Chem.* **2022**, *68*, 104-12. DOI
52. Wang, C.; Yao, Q.; Wang, M.; et al. Highly conductive hierarchical TiO_2 micro-sheet enables thick electrodes in sodium storage. *Adv. Funct. Mater.* **2024**, *34*, 2301996. DOI
53. Guan, S.; Fan, Q.; Shen, Z.; Zhao, Y.; Sun, Y.; Shi, Z. Heterojunction TiO_2@$TiOF_2$ nanosheets as superior anode materials for sodium-ion batteries. *J. Mater. Chem. A.* **2021**, *9*, 5720-9. DOI
54. Xu, X.; Chen, B.; Hu, J.; et al. Heterostructured TiO_2 spheres with tunable interiors and shells toward improved packing density and pseudocapacitive sodium storage. *Adv. Mater.* **2019**, *31*, e1904589. DOI PubMed
55. Meng, W.; Dang, Z.; Li, D.; Jiang, L.; Fang, D. Interface and defect engineered titanium-base oxide heterostructures synchronizing high-rate and ultrastable sodium storage. *Adv. Energy. Mater.* **2022**, *12*, 2201531. DOI
56. Zhao, Q.; Xia, Z.; Qian, T.; et al. PVP-assisted synthesis of ultrafine transition metal oxides encapsulated in nitrogen-doped carbon nanofibers as robust and flexible anodes for sodium-ion batteries. *Carbon* **2021**, *174*, 325-34. DOI
57. Hou, T.; Liu, B.; Sun, X.; et al. Covalent coupling-stabilized transition-metal sulfide/carbon nanotube composites for lithium/sodium-ion batteries. *ACS. Nano.* **2021**, *15*, 6735-46. DOI PubMed
58. Chen, Y.; Liu, H.; Guo, X.; et al. Bimetallic sulfide SnS_2/FeS_2 nanosheets as high-performance anode materials for sodium-ion batteries. *ACS. Appl. Mater. Interfaces.* **2021**, *13*, 39248-56. DOI PubMed
59. Muhammad M, Liu Y, Sheng L, Haruna B, Hu X, Wen Z. Phase engineering of nickel-based sulfides toward robust sodium-ion batteries. *J. Colloid. Interface. Sci.* **2023**, *646*, 245-53. DOI PubMed
60. Wang, X.; Zhang, X.; Chen, Y.; Dong, J.; Zhao, J. Optimizing electron spin-polarized states of $MoSe_2$/Cr_2Se_3 heterojunction-embedded carbon nanospheres for superior sodium/potassium-ion battery performances. *Small* **2024**, *20*, e2312130. DOI PubMed
61. Chen, H.; Tian, P.; Fu, L.; Wan, S.; Liu, Q. Hollow spheres of solid solution $Fe_7Ni_3S_{11}$/CN as advanced anode materials for sodium ion batteries. *Chem. Eng. J.* **2022**, *430*, 132688. DOI
62. Wang, Z.; Dong, K.; Wang, D.; et al. Constructing N-doped porous carbon confined FeSb alloy nanocomposite with Fe-N-C coordination as a universal anode for advanced Na/K-ion batteries. *Chem. Eng. J.* **2020**, *384*, 123327. DOI
63. Ma, W.; Wang, J.; Gao, H.; et al. A mesoporous antimony-based nanocomposite for advanced sodium ion batteries. *Energy. Storage. Mater.* **2018**, *13*, 247-56. DOI
64. Edison, E.; Sreejith, S.; Ren, H.; Lim, C. T.; Madhavi, S. Microstructurally engineered nanocrystalline Fe–Sn–Sb anodes: towards

stable high energy density sodium-ion batteries. *J. Mater. Chem. A.* **2019**, *7*, 14145-52. DOI

65. Chen, L.; He, X.; Chen, H.; Huang, S.; Wei, M. N-doped carbon encapsulating Bi nanoparticles derived from metal–organic frameworks for high-performance sodium-ion batteries. *J. Mater. Chem. A.* **2021**, *9*, 22048-55. DOI
66. Gao, H.; Niu, J.; Zhang, C.; Peng, Z.; Zhang, Z. A dealloying synthetic strategy for nanoporous bismuth-antimony anodes for sodium ion batteries. *ACS. Nano.* **2018**, *12*, 3568-77. DOI PubMed
67. Ma, W.; Yin, K.; Gao, H.; Niu, J.; Peng, Z.; Zhang, Z. Alloying boosting superior sodium storage performance in nanoporous tin-antimony alloy anode for sodium ion batteries. *Nano. Energy.* **2018**, *54*, 349-59. DOI
68. Lei, S.; Qiu, M.; Hu, X.; et al. Heteroatomic phosphorus selenides molecules encapsulated in porous carbon as a highly reversible anode for sodium-ion batteries. *Mater. Today. Nano.* **2023**, *22*, 100344. DOI
69. Xu, Z.; Wang, J.; Guo, Z.; et al. The role of hydrothermal carbonization in sustainable sodium-ion battery anodes. *Adv. Energy. Mater.* **2022**, *12*, 2200208. DOI
70. Lu, Y.; Zhao, C.; Qi, X.; et al. Pre-oxidation-tuned microstructures of carbon anodes derived from pitch for enhancing Na storage performance. *Adv. Energy. Mater.* **2018**, *8*, 1800108. DOI
71. Zhao, J.; He, X.; Lai, W.; et al. Catalytic defect-repairing using manganese ions for hard carbon anode with high-capacity and high-initial-coulombic-efficiency in sodium-ion batteries. *Adv. Energy. Mater.* **2023**, *13*, 2300444. DOI
72. Wang, J.; Zhao, J.; He, X.; Qiao, Y.; Li, L.; Chou, S. Hard carbon derived from hazelnut shell with facile HCl treatment as high-initial-coulombic-efficiency anode for sodium ion batteries. *Sustainable. Mater. Technol.* **2022**, *33*, e00446. DOI
73. Meng, Q.; Lu, Y.; Ding, F.; Zhang, Q.; Chen, L.; Hu, Y. Tuning the closed pore structure of hard carbons with the highest Na storage capacity. *ACS. Energy. Lett.* **2019**, *4*, 2608-12. DOI
74. Kamiyama, A.; Kubota, K.; Igarashi, D.; et al. MgO-template synthesis of extremely high capacity hard carbon for Na-ion battery. *Angew. Chem. Int. Ed. Engl.* **2021**, *60*, 5114-20. DOI PubMed PMC
75. Li, Y.; Lu, Y.; Meng, Q.; et al. Regulating pore structure of hierarchical porous waste cork-derived hard carbon anode for enhanced Na storage performance. *Adv. Energy. Mater.* **2019**, *9*, 1902852. DOI
76. Li, Q.; Liu, X.; Tao, Y.; et al. Sieving carbons promise practical anodes with extensible low-potential plateaus for sodium batteries. *Natl. Sci. Rev.* **2022**, *9*, nwac084. DOI PubMed PMC
77. Ma, L.; Gao, X.; Zhang, W.; et al. Ultrahigh rate capability and ultralong cycling stability of sodium-ion batteries enabled by wrinkled black titania nanosheets with abundant oxygen vacancies. *Nano. Energy.* **2018**, *53*, 91-6. DOI
78. Han, M.; Zou, Z.; Liu, J.; et al. Pressure-induced defects and reduced size endow TiO_2 with high capacity over 20 000 cycles and excellent fast-charging performance in sodium ion batteries. *Small* **2024**, *20*, e2312119. DOI PubMed
79. Hwang, J.; Du, H.; Yun, B.; et al. Carbon-free TiO_2 microspheres as anode materials for sodium ion batteries. *ACS. Energy. Lett.* **2019**, *4*, 494-501. DOI
80. Yang, J.; Huang, M.; Xu, L.; Xia, X.; Peng, C. Self-assembled titanium-deficient undoped anatase TiO_2 nanoflowers for ultralong-life and high-rate Li^+/Na^+ storage. *Chem. Eng. J.* **2022**, *445*, 136638. DOI
81. Lan, K.; Liu, L.; Zhang, J. Y.; et al. Precisely designed mesoscopic titania for high-volumetric-density pseudocapacitance. *J. Am. Chem. Soc.* **2021**, *143*, 14097-105. DOI PubMed
82. Xia, Q.; Liang, Y.; Lin, Z.; et al. Confining ultrathin 2D superlattices in mesoporous hollow spheres renders ultrafast and high-capacity Na-ion storage. *Adv. Energy. Mater.* **2020**, *10*, 2001033. DOI
83. Liu, S.; Niu, K.; Chen, S.; et al. TiO_2 bunchy hierarchical structure with effective enhancement in sodium storage behaviors. *Carbon. Energy.* **2022**, *4*, 645-53. DOI
84. Yang, D.; Xu, B.; Zhao, Q.; Zhao, X. S. Three-dimensional nitrogen-doped holey graphene and transition metal oxide composites for sodium-ion batteries. *J. Mater. Chem. A.* **2019**, *7*, 363-71. DOI
85. Khan, R.; Yan, W.; Ahmad, W.; et al. Role of moderate strain engineering in Nickel Sulfide anode for advanced sodium-ion batteries. *J. Alloys. Compd.* **2023**, *963*, 171196. DOI
86. Li, R.; Dong, W.; Pan, J.; Huang, F. Micrometer-sized, dual-conductive MoO_2/β-MoO_{3-x} mosaics for high volumetric capacity Li/Na-ion batteries. *Small. Methods.* **2021**, *5*, e2100765. DOI PubMed
87. Wang, B.; Li, F.; Wang, X.; Wang, G.; Wang, H.; Bai, J. Mn_3O_4 nanotubes encapsulated by porous graphene sheets with enhanced electrochemical properties for lithium/sodium-ion batteries. *Chem. Eng. J.* **2019**, *364*, 57-69. DOI
88. Zhang, K.; Xiong, F.; Zhou, J.; Mai, L.; Zhang, L. Universal construction of ultrafine metal oxides coupled in N-enriched 3D carbon nanofibers for high-performance lithium/sodium storage. *Nano. Energy.* **2020**, *67*, 104222. DOI
89. Xu, M.; Xia, Q.; Yue, J.; et al. Rambutan-like hybrid hollow spheres of carbon confined Co_3O_4 nanoparticles as advanced anode materials for sodium-ion batteries. *Adv. Funct. Mater.* **2019**, *29*, 1807377. DOI
90. Zhao, Y.; Wang, F.; Wang, C.; et al. Encapsulating highly crystallized mesoporous Fe_3O_4 in hollow N-doped carbon nanospheres for high-capacity long-life sodium-ion batteries. *Nano. Energy.* **2019**, *56*, 426-33. DOI
91. Cao, L.; Gao, X.; Zhang, B.; Ou, X.; Zhang, J.; Luo, W. B. Bimetallic sulfide Sb_2S_3@FeS_2 hollow nanorods as high-performance anode materials for sodium-ion batteries. *ACS. Nano.* **2020**, *14*, 3610-20. DOI PubMed
92. Liu, J.; Li, Y.; Chen, Z.; et al. Polyoxometalate cluster-incorporated high entropy oxide sub-1 nm nanowires. *J. Am. Chem. Soc.* **2022**, *144*, 23191-7. DOI PubMed
93. Yang, H.; Chen, L. W.; He, F.; et al. Optimizing the void size of yolk-shell Bi@Void@C nanospheres for high-power-density sodium-ion batteries. *Nano. Lett.* **2020**, *20*, 758-67. DOI PubMed

94. Fan, X.; Han, J.; Ding, Y.; et al. 3D nanowire arrayed Cu current collector toward homogeneous alloying anode deposition for enhanced sodium storage. *Adv. Energy. Mater.* **2019**, *9*, 1900673. DOI
95. Dang, J.; Zhu, R.; Zhang, S.; et al. Bean pod-like SbSn/N-doped carbon fibers toward a binder free, free-standing, and high-performance anode for sodium-ion batteries. *Small* **2022**, *18*, e2107869. DOI PubMed
96. Song, Z.; Wang, G.; Chen, Y.; Lu, Y.; Wen, Z. In situ three-dimensional cross-linked carbon nanotube-interspersed SnSb@CNF as freestanding anode for long-term cycling sodium-ion batteries. *Chem. Eng. J.* **2023**, *463*, 142289. DOI
97. Kim, Y. H.; An, J. H.; Kim, S. Y.; et al. Enabling 100C fast-charging bulk Bi anodes for Na-ion batteries. *Adv. Mater.* **2022**, *34*, e2201446. DOI PubMed
98. Eaves-Rathert, J.; Moyer-Vanderburgh, K.; Wolfe, K.; Zohair, M.; Pint, C. L. Leveraging impurities in recycled lead anodes for sodium-ion batteries. *Energy. Storage. Mater.* **2022**, *53*, 552-8. DOI
99. Fang, H.; Gao, S.; Ren, M.; et al. Dual-function presodiation with sodium diphenyl ketone towards ultra-stable hard carbon anodes for sodium-ion batteries. *Angew. Chem. Int. Ed. Engl.* **2023**, *62*, e202214717. DOI PubMed
100. Bai, P.; Han, X.; He, Y.; et al. Solid electrolyte interphase manipulation towards highly stable hard carbon anodes for sodium ion batteries. *Energy. Storage. Mater.* **2020**, *25*, 324-33. DOI
101. Jin, Y.; Xu, Y.; Xiao, B.; et al. Stabilizing interfacial reactions for stable cycling of high-voltage sodium batteries. *Adv. Funct. Mater.* **2022**, *32*, 2204995. DOI
102. Jin, Y.; Xu, Y.; Le, P. M. L.; et al. Highly reversible sodium ion batteries enabled by stable electrolyte-electrode interphases. *ACS. Energy. Lett.* **2020**, *5*, 3212-20. DOI
103. Li, K.; Zhang, J.; Lin, D.; et al. Evolution of the electrochemical interface in sodium ion batteries with ether electrolytes. *Nat. Commun.* **2019**, *10*, 725. DOI PubMed PMC
104. Meng, W.; Dang, Z.; Li, D.; Jiang, L. Long-cycle-life sodium-ion battery fabrication via a unique chemical bonding interface mechanism. *Adv. Mater.* **2023**, *35*, e2301376. DOI PubMed
105. Xu, Z.; Lim, K.; Park, K.; Yoon, G.; Seong, W. M.; Kang, K. Engineering solid electrolyte interphase for pseudocapacitive anatase TiO_2 anodes in sodium-ion batteries. *Adv. Funct. Mater.* **2018**, *28*, 1802099. DOI
106. Cha, G.; Mohajernia, S.; Nguyen, N. T.; et al. Li^+ pre-insertion leads to formation of solid electrolyte interface on TiO_2 nanotubes that enables high-performance anodes for sodium ion batteries. *Adv. Energy. Mater.* **2020**, *10*, 1903448. DOI
107. Li, Q.; Cao, Z.; Cheng, H.; et al. Electrolyte boosting microdumbbell-structured alloy/metal oxide anode for fast-charging sodium-ion batteries. *ACS. Mater. Lett.* **2022**, *4*, 2469-79. DOI
108. Yang, J.; Guo, X.; Gao, H.; et al. A high-performance alloy-based anode enabled by surface and interface engineering for wide-temperature sodium-ion batteries. *Adv. Energy. Mater.* **2023**, *13*, 2300351. DOI
109. Chu, C.; Zhou, L.; Cheng, Y.; et al. Ultralow-concentration (0.1M) electrolyte for stable bulk alloy (Sn, Bi) anode in sodium-ion battery via regulating anions structure. *Chem. Eng. J.* **2024**, *482*, 148915. DOI
110. Huang, J.; Guo, X.; Du, X.; et al. Nanostructures of solid electrolyte interphases and their consequences for microsized Sn anodes in sodium ion batteries. *Energy. Environ. Sci.* **2019**, *12*, 1550-7. DOI
111. Wu, X.; Li, Z.; Feng, W.; et al. Insights into electrolyte-induced temporal and spatial evolution of an ultrafast-charging Bi-based anode for sodium-ion batteries. *Energy. Storage. Mater.* **2024**, *66*, 103219. DOI
112. Zhao, B.; Han, J.; Liu, B.; Zhang, S. L.; Guan, B. Hierarchical metal–organic framework nanoarchitectures for catalysis. *Chem. Synth.* **2024**, *4*, 41. DOI
113. Peng, Y.; Tan, Q.; Huang, H.; et al. Customization of functional MOFs by a modular design strategy for target applications. *Chem. Synth.* **2022**, *2*, 15. DOI
114. Li, H.; Li, C.; Wang, Y.; et al. Selenium confined in ZIF-8 derived porous carbon@MWCNTs 3D networks: tailoring reaction kinetics for high performance lithium-selenium batteries. *Chem. Synth.* **2022**, *2*, 8. DOI
115. Su, Y.; Yuan, G.; Hu, J.; et al. Recent progress in strategies for preparation of metal-organic frameworks and their hybrids with different dimensions. *Chem. Synth.* **2022**, *3*, 1. DOI
116. Wang, R.; Zhao, J.; Fang, Q.; Qiu, S. Advancements and applications of three-dimensional covalent organic frameworks. *Chem. Synth.* **2024**, *4*, 29. DOI
117. Li, X.; Geng, K.; Fu, S.; Jin, E. Molecular engineering toward large pore-sized covalent organic frameworks. *Chem. Synth.* **2024**, *4*, 15. DOI
118. Yin, X.; Sarkar, S.; Shi, S.; et al. Recent progress in advanced organic electrode materials for sodium-ion batteries: synthesis, mechanisms, challenges and perspectives. *Adv. Funct. Mater.* **2020**, *30*, 1908445. DOI
119. Lee, J.; Kim, Y.; Park, S.; et al. Sodium-coordinated polymeric phthalocyanines as stable high-capacity organic anodes for sodium-ion batteries. *Energy. Environ. Mater.* **2023**, *6*, e12468. DOI
120. Liu, Y.; Yao, Z.; Vanaphuti, P.; et al. Stable fast-charging sodium-ion batteries achieved by a carbomethoxy-modified disodium organic material. *Cell. Rep. Phys. Sci.* **2023**, *4*, 101240. DOI